## Carbon ion implantation for electron compensation in epitaxial scandium nitride

Sourav Rudra , 1,2,\* Dheemahi Rao , 1,2,\* Sneha Kobri M , 1,2 Aritra Dey , 1,2 Renuka Karanje , 1,2 Prasanna Das , 1,2 Subhajit Manna , 1,2 Madhusmita Baral , 3,4 Bhupesh Yadav , 1,2 Ashalatha Indiradevi Kamalasanan Pillai , 5 Magnus Garbrecht , 5 Mukul Gupta , 6 Satyaprakash Sahoo , 4,7 Tapas Ganguli , 3,4 and Bivas Saha , 1,2,8,† Chemistry and Physics of Materials Unit, Jawaharlal Nehru Centre for Advanced Scientific Research, Bangalore 560064, India International Centre for Materials Science, Jawaharlal Nehru Centre for Advanced Scientific Research, Bangalore 560064, India Raja Ramanna Centre for Advanced Technology, Indore 452013, India Homi Bhabha National Institute, Training School Complex, Anushakti Nagar, Mumbai 400094, India Sydney Microscopy and Microanalysis, The University of Sydney, Camperdown NSW 2006, Australia 
GUGC-DAE Consortium for Scientific Research, Khandwa Road, Indore-452017, India 
Taboratory for Low Dimensional Materials, Institute of Physics, Bhubaneswar-751005, India 
School of Advanced Materials and Sheikh Saqr Laboratory, Jawaharlal Nehru Centre for Advanced Scientific Research, Bangalore 560064, India

(Received 17 March 2025; accepted 10 September 2025; published 6 October 2025)

Scandium nitride, an emerging rocksalt indirect bandgap semiconductor, has attracted much interest recently for thermoelectricity, infrared plasmon and phonon-polaritons, neuromorphic computing, and Schottky diode device applications. As-deposited ScN thin films exhibit a high electron concentration due to oxygen impurities and nitrogen vacancies. Magnesium hole doping is the only effective method to compensate for high electron concentration and achieve *p*-type ScN. However, it is crucial to identify other hole doping strategies for ScN to promote its diverse applications. Here, we show conclusive experimental evidence of ion-implanted carbon as a hole dopant in ScN, reducing electron concentration by more than an order of magnitude. Through comprehensive spectroscopic and microscopic characterization techniques and first-principles modeling, we show that carbon occupies nitrogen sites in ScN for low dopant concentrations, leading to a hole-doping nature that compensates for ScN's high electron concentration. However, as carbon concentration increases, its hole doping ability reduces due to the formation of donor-type defect complexes identified from first-principles modeling analysis. Our work marks the experimental demonstration of hole doping in ScN with carbon ion-implantation and presents a pathway to tune the electron concentration in ScN for device applications.

## DOI: 10.1103/b5x8-c1bl

### I. INTRODUCTION

Compensation for high electron concentration caused by native donors or foreign impurities is vital for optimizing the properties of degenerate semiconductors [1–3]. Effective compensation techniques, such as hole doping, can transform a semiconductor's electronic transport behavior from n-type to p-type [4,5], enabling precise control over plasmon and phonon-polariton resonances across short- and long-wavelength infrared spectral ranges [6,7]. Additionally, compensating high carrier concentration is key to optimizing the Seebeck coefficient and electrical conductivity, critical for achieving high thermoelectric power factors and advancing the design of electronic, optoelectronic, and power electronic devices [8,9]. This challenge is particularly important for nitride semiconductors, as they often exhibit degenerate semiconducting properties due to the presence of native nitrogen vacancies and contamination from impurities such as oxygen or halogens [10–18]. Addressing this issue through donor compensation and hole doping strategies is critical for

unlocking their full potential and ensuring widespread applicability in cutting-edge technologies.

Scandium nitride (ScN), a promising group 3 rocksalt transition metal pnictide, has emerged as a focal point of research due to its versatile properties and wide-ranging applications. Renowned for its potential in thermoelectric energy conversion [19–21], ScN hosts short- and long-wavelength infrared plasmonics, phonon-polaritons [22], brain-inspired neuromorphic computing functionalities [23], and rectification across the Schottky barriers [24]. Like other transition metal nitrides (TMNs), ScN shows exceptional corrosion resistance, mechanical hardness, and an impressively high melting temperature of  $\sim$ 2600 °C [25,26]. The similarity of ScN's crystal structure and the nearly matched lattice constants with metallic TMNs such as hafnium nitride (HfN) and zirconium nitride (ZrN) has paved the way for ScN-based epitaxial metal/semiconductor superlattices [27], enabling thermionic energy conversion and optical hyperbolic metamaterials [28]. Additionally, ScN's near-perfect lattice-matching with GaN has been leveraged to grow nearly dislocation-free GaN epilayers, offering exciting possibilities in light-emission and power electronic semiconductor device technology [29–31]. Beyond its standalone applications, ScN forms solid-state alloys with group 13 nitrides, enabling the deposition of

<sup>\*</sup>These authors contributed equally to this work.

<sup>†</sup>Contact author: bsaha@jncasr.ac.in; bivas.mat@gmail.com

wurtzite-phase thin films such as  $Al_xSc_{1-x}N$  and  $Ga_xSc_{1-x}N$  exhibiting extraordinary piezoelectric and ferroelectric properties, which is currently an exciting research field in both academia and industry, with a wide range of applications in sensors, actuators, and energy harvesting devices [32–36]. Theoretical studies further highlight ScN's potential as a barrier material for magnetic tunnel junctions, highlighting its pivotal role in future spintronic devices [37].

Epitaxial ScN thin films deposited with an ultrahigh vacuum (UHV) magnetron sputtering or molecular beam epitaxy (MBE) exhibit a high *n*-type concentration in the  $10^{20}$  – 10<sup>21</sup> cm<sup>-3</sup> range [11,38]. Such large carrier concentrations in as-deposited films originate due to unwanted substitutional oxygen in the nitrogen site (O<sub>N</sub>) as an impurity and native defects such as nitrogen vacancies that reduce the electron mobility to a moderate range of  $\sim 60-130 \,\mathrm{cm^2/V.s}$ with dominant ionized-impurity scattering [39]. Such large carrier concentrations and the moderate mobility lead to a high room-temperature electrical conductivity of 1759 Scm<sup>-1</sup> and a high Seebeck coefficient of −175 µV/K at 950 K in epitaxial ScN thin films, resulting in a high thermoelectric power factor of  $\sim (2.3-3.3) \times 10^{-3} \,\mathrm{W/mK^2}$  in the temperature range of 500 to 600 K [20,40]. The degenerate electronic nature of ScN is also utilized to demonstrate low-loss and high figure-of-merit short wavelength infrared (SWIR) plasmon polaritons, with the epsilon near zero resonance in the 1.5-2.5 µm spectral range [22]. Akin to GaN, substitutional magnesium (Mg) on Sc sites has been found to act as an effective hole dopant in ScN and reduce the electron concentration, eventually leading to p-type ScN films [41]. A maximum hole concentration of  $\sim 2.2 \times 10^{20} \, \mathrm{cm}^{-3}$  and moderate hole mobility of  $\sim 22 \text{ cm}^2/\text{V.s}$  are also achieved at room temperature in p-type ScN films [41]. Large hole concentrations and a rigid-band electronic structure of ScN for unintentional oxygen (n-type) and intentional magnesium (p-type) doping also lead to a high thermoelectric power factor in p-type ScN thin films [42]. Moreover, intentionally undoped (n-type) and Mg-hole-doped ScN films show persistent negative and positive photoconductivity, respectively, which are also used to develop optoelectronic artificial synaptic devices that mimic biological neurons' functionalities [23].

While Mg hole doping is a well-established technique to reduce the excess electron concentration in ScN thin films, Mg-ionized impurity also scatters carriers and reduces mobility [43]. Recent research exhibits several orders of magnitude increase in the resistivity of Mg-doped ScN due to quasiclassical Anderson localization [44]. Moreover, for a widespread application of ScN, it is crucial to achieve flexibility in terms of efficient hole dopants that reduce its carrier concentrations. Therefore, there is a pressing need to find alternative hole dopants in ScN that reduce the carrier concentration significantly. Yet, until now, no other hole dopants except Mg have been identified for ScN. Here, we show the first conclusive experimental demonstration of carbon ion-implanted carrier compensation and hole doping in epitaxial ScN thin films.

The valence shell electron difference between C and N suggests that substitutional C on N sites  $(C_N)$  should act as an acceptor dopant in ScN, which is further justified by the *ab initio* density functional theory (DFT) calculations [21]. The theoretical calculation also shows that the  $C_N$  formation

energies in ScN are positive and relatively high,  $\sim 3-4.5$  eV [45]. Moreover, the electronic nature of carbon doping in ScN is similar to the C-doping in GaN, which has a much deeper acceptor state with an electronic activation energy of 0.9 eV [46,47]. Recent hybrid functional DFT calculation has attributed blue luminescence in C-doped GaN to interstitial hydrogen atoms  $H_i$  bonded to  $C_N$  or an  $O_N C_N - H_i$  defect complex, and yellow luminescence is presumed to appear at 2.25 eV from  $C_N$  or  $O_N C_N$  [48]. The lattice position of C in the N site of GaN is further experimentally demonstrated using polarized Fourier-transform infrared and Raman spectroscopies [49].

While the formation energy and position of the defect states of C<sub>N</sub> in ScN are determined [21,45], not much information is available on the defect complexes in ScN. The recently published report shows that defect complexes comprising of Sc-vacancy (V<sub>Sc</sub>) and hydrogen or oxygen are energetically more stable in ScN than individual  $V_{Sc}$  [50]. Nevertheless, the high positive formation energy of C<sub>N</sub> in ScN could be a significant impediment in realizing hole doping of ScN with C and may explain our unsuccessful experimental attempts to compensate for high background electron concentration in ScN with C doping through cosputtering inside the UHV magnetron sputtering, even at high growth temperatures (see Supplemental Material (SM) Sec. II for details [51]). Therefore, the nonequilibrium ion-beam irradiation/implantation method is used to overcome the thermodynamic barrier for C<sub>N</sub> formation and achieve carbon hole doping in ScN thin films.

#### II. EXPERIMENTAL AND COMPUTATIONAL METHODS

## A. Growth and experimental methods

Epitaxial ScN thin films are deposited on  $1\,\mathrm{cm} \times 1\,\mathrm{cm}$  single-crystalline MgO (001) substrates inside a UHV chamber with DC magnetron sputtering at a base pressure of  $1\times 10^{-9}$  Torr at  $800\,^{\circ}\mathrm{C}$  substrate temperature. Ar (99.99999%) and  $N_2$  (99.99999%) gas ratios were kept at 9 and 2 sccm, respectively, maintaining 10 mTorr deposition pressure during the growth inside the sputtering chamber. Before the deposition, substrates were ultrasonicated in acetone and methanol for 10 minutes each, followed by thermal annealing at  $800\,^{\circ}\mathrm{C}$  for 30 minutes to remove adsorbed contaminants from the substrates. The Sc target (99.995% purity) was presputtered for 30 minutes to remove the surface impurities. The films were deposited for 130 minutes with an average growth rate of  $\sim 1\,\mathrm{nm/min}$  and a thickness of approximately 130 nm.

The Stopping and Range of Ions in Matter (SRIM) simulation is carried out to estimate the suitable implantation energy to obtain carbon ions constricted to the specific thickness of the ScN film (details in Sec. IX in SM [51]). Based on the simulated estimate, after the film deposition, single-ionized carbon atoms (C<sup>-</sup>) are implanted at room temperature with the beam energy of 35 keV at different dosages starting from  $5 \times 10^{13}$  cm<sup>-2</sup> to  $5 \times 10^{16}$  cm<sup>-2</sup>. A pristine ScN sample without any C-implantation is used as a reference to study the changes after implantation. The pristine and C-implanted ScN films are further characterized by several spectroscopic, electrical, and microstructural techniques.

While HRXRD, HRTEM, SEM, and AFM are employed for scrutinizing the structural variations in C-implanted films with respect to the nonimplanted ScN films, temperature-dependent Hall and Seebeck measurements are used for analyzing the electrical variations. The changes in atomic coordination and, thus, the band levels are analyzed with XPS, UPS, and XAS. Variable-angle spectroscopic ellipsometry is further utilized for investigating the samples. Details of all these characterization techniques are provided in the SM Sec. I [51] (see also Refs. [52,53] therein).

#### **B.** Computational methods

First-principles DFT calculations as implemented in the Quantum ESPRESSO package [54], are performed to determine the formation energies and electronic density of states for several neutral point defects and defect complexes due to the implanted Carbon. Projected-augmented-wave (PAW) pseudopotentials [55] with PBE parametrization of generalized gradient approximation (GGA) exchange-correlation functional [56] is used within the DFT+U framework to correct the underestimation of the bandgap [57,58]. The Hubbard U of 3.5 eV with an orthoatomic projection scheme is applied to the Sc 3d orbitals to correct the bandgap. The kinetic energy cut-off of 85 Ry and Marzari-Vanderbilt smearing [59] with a smearing width of 0.002 Ry is used for all the calculations. A  $2 \times 2 \times 2$  supercell containing 64 atoms is used for the defect calculations. The Brillouin zone was sampled with a  $\Gamma$ -centered k-mesh grid of  $16 \times 16 \times 16$  for the primitive cell and  $8 \times 8 \times 8$  for the supercell, including defects. The atomic positions and lattice parameters are relaxed properly using the Davidson diagonalization algorithm until the forces on the individual atoms become less than 0.025 eV/Å. The DFT+U optimized lattice parameter of pristine ScN is 4.56 Å.

The formation energy  $E_f(\text{def})$  of neutral point defects and defect complexes is calculated using the Zhang-Northrup scheme [60],

$$E_f(\text{def}) = E_{\text{tot}}(\text{def}) - E_{\text{tot}}(\text{pristine}) + \sum_i x_i \mu_i,$$

where  $E_{tot}(def)$  and  $E_{tot}(pristine)$  are the total energies of the supercell containing the defects and the pristine supercell, respectively.  $x_i$  is the number of atomic species added  $(x_i < 0)$  or removed  $(x_i > 0)$  from the pristine supercell to create a defect supercell and  $\mu_i$  is the chemical potential of the element added or removed. Formation energies are calculated for all the defects under the nitrogen-rich condition, in which the nitrogen chemical potential is represented as  $\mu_N = \frac{1}{2} E_{\text{tot}}(N_2)$ , where  $E_{\text{tot}}(N_2)$  is the total energy of  $N_2$ molecule, calculated by considering one  $N_2$  molecule inside a supercell with a vacuum of 25 Å in each direction. As oxygen will always be present in ScN, we have considered the defect complexes, including oxygen point defects, and calculated the defect formation energies for oxygen-rich and oxygen-poor conditions. In the oxygen-rich condition,  $\mu_O = \frac{1}{2} E_{\text{tot}}(O_2)$  and in an oxygen-poor condition  $\mu_O = \frac{1}{3}(E_{\text{tot}}(Sc_2O_3) - 2 \times \mu_{Sc}),$ where  $E_{\text{tot}}(O_2)$  is the total energy of  $O_2$  molecule, calculated by considering one  $O_2$  molecule inside a supercell with a vacuum of 25 Å in each direction.  $E_{\text{tot}}(Sc_2O_3)$  is the total energy of pristine cubic  $Sc_2O_3$  which is the stable oxide of Sc,  $\mu_{Sc}$  is the chemical potential of Sc in the stable metallic form [61]. In the nitrogen-rich condition, the chemical potential of Sc is represented as,  $\mu_{Sc}^{N-{\rm rich}}=E_{\rm primitive}(ScN)-\mu_N$ . The thermodynamic stability of both ScN and  $Sc_2O_3$  are further calculated from formation enthalpy per formula unit (fu)  $\Delta H^f$  such as  $\Delta H^f(ScN)=E_{\rm primitive}(ScN)-\mu_{Sc}-\mu_N$  and  $\Delta H^f(Sc_2O_3)=E_{\rm primitive}(Sc_2O_3)-2\times\mu_{Sc}-3\times\frac{1}{2}E_{\rm tot}(O_2)$ .

Furthermore, the charged defect formation energies are calculated as a function of the Fermi level position to gain a comprehensive understanding of the defect physics in ScN, using the screened Heyd, Scuseria, and Ernzerhof (HSE06) hybrid functional [62,63] with GGA exchange-correlation and PAW pseudopotentials [64] as implemented in the Vienna Ab initio simulation Package (VASP) [65]. The formation energies are calculated using the recently developed Python package PyDefect [66–69], integrated with VASP. The choice of hybrid functional over the local or semilocal local density approximation (LDA) [70,71] or GGA [56] functionals is essential for correctly capturing the defect formation energies in semiconductors [72]. Among possible hybrid functionals, HSE06 is the most popular choice and widely used in oxides and nitrides for the accurate determination of the defect formation energies and transition levels [66,72,73].

A  $2 \times 2 \times 2$  supercell containing 64 atoms is considered for the pristine and charged defect calculations, using a 2 ×  $2 \times 2$  Monkhorst-Pack k-point grid [74] and energy cutoff of 550 eV. The bandgap of ScN is obtained as 0.79 eV for an exact exchange value of 0.25. The dielectric constants are calculated using the PBE+U method [57] with a U<sub>eff</sub> of 3.5 eV, resulting in a bandgap of 0.74 eV. The PBE+U calculated electronic and ionic dielectric constants yield 8.97 and 20.21, respectively, further used in the correction of finite supercell size error. Spin-polarization is included in all the defect calculations. As the structural relaxation of the supercell, containing defects with the hybrid functional is computationally expensive, a computationally cheaper PBE functional is first used for relaxing the atomic positions in the defect supercells until the forces on the individual atoms become less than 0.04 eV/Å, and then the static calculations are performed on the PBE-relaxed structures using the HSE06 hybrid functional to determine the total energies with affordable computational cost. The lattice parameter is kept fixed at the HSE06 optimized bulk value of 4.48 Å for all the defect calculations.

The charged defects formation energies of point defects and defect complexes are calculated as a function of the Fermi level using the following relation [45,75],

$$E_f[D^q] = \{E[D^q] + E_{corr}[D^q]\} - E_P - \sum n_i \mu_i + q(\epsilon_{VBM} + \Delta \epsilon_F),$$

where,  $E[D^q]$  and  $E_P$  are the total energies of the supercell containing the defect D in charge state q, and the pristine supercell, respectively.  $n_i$  is the number of atomic species added  $(n_i > 0)$  or removed  $(n_i < 0)$  from the pristine supercell to create a defect supercell and  $\mu_i$  corresponds to their chemical potentials. The chemical potentials of Sc, N, C, and O in both Sc-rich and N-rich conditions are determined from the HSE06 hybrid functional calculations using referenced competing phases, such as hexagonal Sc,  $O_2$  and  $O_2$  molecules, graphitic

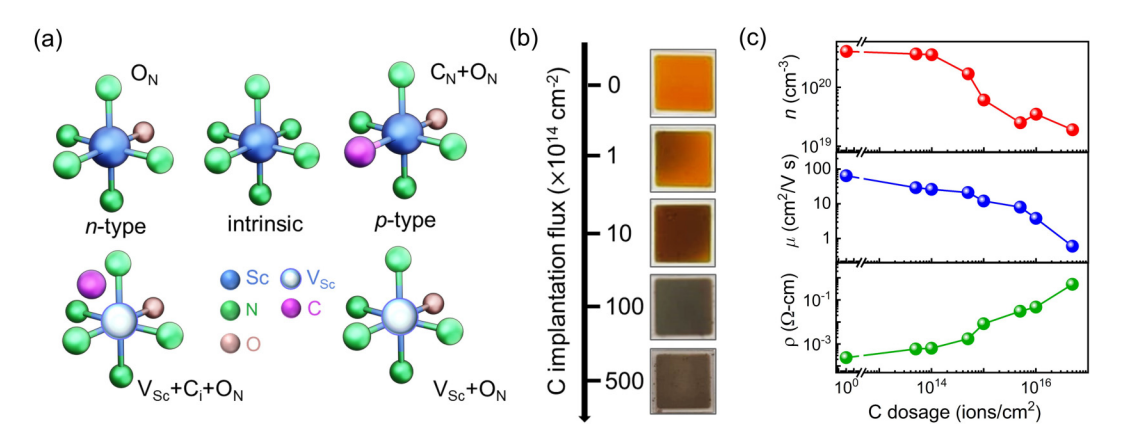


FIG. 1. (a) Schematic of intrinsic and several electronically active *n*-type and *p*-type defects in C-implanted ScN. Depending on the site occupation, Carbon can act as a *p*-type or *n*-type dopant. (b) Optical images of the C-implanted ScN thin film surfaces with different implantation dosages. (c) Variation of the films' electron concentration, mobility, and resistivity with increasing C-implantation dosage in ScN film. With the highest implantation dosage, the carrier concentration in ScN is reduced by more than an order of magnitude.

C, cubic Sc<sub>2</sub>O<sub>3</sub>, trigonal Sc<sub>2</sub>C, tetragonal Sc<sub>3</sub>C<sub>4</sub>, and cubic  $Sc_4C_3$ . The  $\epsilon_{VBM}$  refers to the energy of the valence band maxima (VBM) and  $\Delta \epsilon_F$  is the Fermi level position with respect to VBM.  $E_{\text{corr}}[D^q]$  represents the energy correction due to the spurious electrostatic interaction of the defect charge with its periodic counterpart, arising from the finite supercell size. An extended Freysoldt-Neugebauer-Van de Walle (FNV) correction scheme is used to calculate this energy correction term [75,76]. This correction scheme is well established and used quite frequently to determine the formation energies accurately, even with the supercell containing 64 atoms [45,50,75]. We have used expensive HSE06 hybrid functional calculations for all the defects and pristine supercells, as well as the determination of chemical potentials, in order to determine the formation energies accurately. However, the calculated defect formation energy needs an additional correction on top of the FNV correction, as it cannot completely remove the finite size effect due to the spilling out of the defect charges, especially important for higher charged defects [45]. The FNV corrected energies are assumed to scale with the number of atoms in the pristine supercell as

$$E_f^{FNV}[D^q] = q^2 a N_{\text{atom}}^{-1} + b[D^q],$$

where  $N_{\text{atom}}$  is the total number of atoms in the supercell expanded isotropically along the cell vectors without introducing the defect D, a is the fitting parameter independent of the defect D and its charge state, and  $b[D^q]$  is the defect formation energy of  $D^q$  corresponding to an infinite supercell. Due to the computational limitation,  $a = 5.70 \, \text{eV}/e^2$  is adopted, as reported in the previous literature of ScN based on HSE06 hybrid functional [45]. The correct formation energies are determined by subtracting  $q^2 a N_{\text{atom}}^{-1}$  from the FNV corrected energies. In addition to the 64-atom supercell calculations presented, we have also performed calculations using a 96-atom supercell to further confirm that finite-size effects do not significantly influence the extended FNV corrected formation energies (see Fig. S15).

Finally, x-ray absorption near edge spectra (XANES) of N K-edge and Sc  $L_3$ - and  $L_2$ -edges are performed using ab initio full multiple scattering theory as implemented in the FEFF 9.05 code [77]. A self-consistent spherical multipn-tin

scattering potential with Hedin-Lundqvist exchange is used in the simulation. The clusters are constructed from relaxed atomic coordinates obtained from DFT calculations. A cluster of radii 6 Å is used to build the atomic potential and is further extended to 8 Å for the calculation of scattering cross sections.

### III. RESULTS AND DISCUSSION

#### A. Electrical characterization

Schematics of various electronically active point defects in as-deposited and C-implanted ScN [presented in Fig. 1(a)] highlight their ability to dope ScN with n-type or p-type carriers. The as-deposited intentionally undoped ScN is a degenerate semiconductor with a carrier concentration of  $\sim$  $4 \times 10^{20}$  cm<sup>-3</sup> due to unwanted oxygen donor impurities (O<sub>N</sub>) from the target contaminations. As-deposited ScN thin film before implantation appears reddish-yellow, consistent with its direct bandgap of 2.2 eV. However, with increasing Cimplantation dosage, films turn darker, as shown in Fig. 1(b). The carrier concentration, mobility, and resistivity of the as-deposited ScN are  $4 \times 10^{20}$  cm<sup>-3</sup>, 64 cm<sup>2</sup>/V s, and  $2.4 \times$  $10^{-4} \Omega$ -cm, respectively. However, as the C-implantation dose increases, the electron concentration reduces gradually by more than an order of magnitude to  $1.8 \times 10^{19}$  cm<sup>-3</sup> for the highest carbon implantation dosage of  $5 \times 10^{16} \, \text{cm}^{-2}$  studied here [refer to Fig. 1(c)]. According to the theoretical calculations, such a drastic reduction in carrier densities indicates the formation of substitutional C<sub>N</sub> point defects that act as a hole dopant in ScN. However, the compensation rate eventually saturates at a low  $\sim 10^{19}$  cm<sup>-3</sup> electron concentration for implantation dosage above  $5 \times 10^{15} \, \text{cm}^{-2}$ , which highlights possibilities for other donor-type complex defects formation that counteract C<sub>N</sub>'s hole doping ability.

The decrease in the electron concentration with increasing implantation dosage is also associated with a decrease in electron mobility from  $64\,\mathrm{cm^2/V}$  s for pristine ScN to  $\sim 1\,\mathrm{cm^2/V}$  s for  $5\times10^{16}\,\mathrm{cm^{-2}}$  implantation dosage. Such a decrease in electron mobility in the implanted films suggests an increasing strength of carrier scattering from implantation-induced defects such as vacancies, interstitial and substitutional ionized

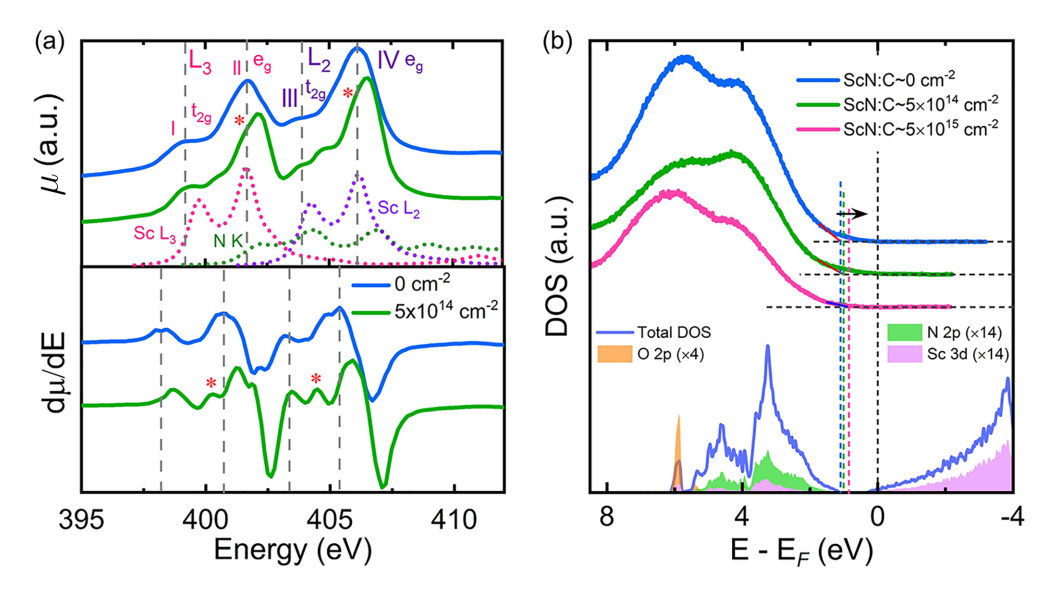


FIG. 2. (a) The Sc-edge SXAS spectra of pristine ScN and C-implanted ScN thin films are presented. The shoulder in the C-implanted sample indicates distortion in the lattice. The first derivative of the spectra in the lower panel shows the absorption edges and shoulder peaks distinctly. The theoretically simulated XANES spectra of pristine ScN are also presented for comparison. The dashed lines indicate the four distinct peak positions of pristine ScN from experimental absorption spectra. (b) The SR-UPS spectra of pristine and C-implanted ScN samples with implantation dosages of  $5 \times 10^{14}$  cm<sup>-2</sup> and  $5 \times 10^{15}$  cm<sup>-2</sup> shows a slight decrease between the Fermi level and the valence band maxima on C-implantation. The theoretically calculated DOS and PDOS of ScN:O<sub>N</sub> are shown below for comparison. The Fermi level of the theoretically calculated DOS is aligned with the experimental one, as shown by the gray-colored dotted line. The valence band edges are also marked for both pristine and C-implanted samples.

impurities, and extended defects like dislocations and vacancy clusters [78]. Due to the combined effect of the decreasing carrier concentration and mobility, the resistivity of the films increases monotonically with increasing implantation dosage. The resistivity of implanted samples with an implantation dose of  $5 \times 10^{16}$  cm<sup>-2</sup> reaches  $\sim 5.1 \times 10^{-1}$   $\Omega$ -cm at room temperature, accounting for a three orders of magnitude increase from the nonimplanted ScN film.

Temperature-dependent resistivity measurements in the 50-400 K range show that compared to its degenerate electronic nature, where resistivity increases by a small amount with increasing temperature in as-deposited ScN, the Cimplanted film with an implantation dosage  $\sim 1 \times 10^{15} \, \text{cm}^{-2}$ exhibits a thermal activation behavior (see Fig. S2(c) in SM Sec. III [51]). Such an activated transport nature appears due to the movement of the Fermi level from inside the conduction band to the bandgap due to acceptor doping. Although the electron concentration decreases by more than an order in C-doped ScN, its temperature dependence remains relatively insensitive (refer to Fig. S2(a)]. Similarly, thermoelectric characterization of the C-implanted films shows a substantial Seebeck coefficient enhancement as a function of temperature [see Fig. S4(b)] due to the reduction in the carrier concentration of the films. Such Seebeck coefficient enhancement has also been observed previously in noble-gas-implanted ScN due to the significant amount of implantation-induced defects [79,80]. Yet, the increase in the Seebeck coefficient is far outweighed by a concomitant increase in the resistivity, which leads to an overall decrease in the thermoelectric power factor, as shown in SM Fig. S4(c) [51].

## B. Electronic structure analysis

The electronic density of states is further probed using soft x-ray absorption spectroscopy (SXAS) for both pristine and C-implanted ScN films and compared with the ab initio calculated XANES of pristine ScN from full multiple scattering (FMS) theory. The soft x-ray absorption spectra of the Sc L-edge of pristine ScN and C-implanted ScN with an implantation dosage of  $5 \times 10^{14}$  cm<sup>-2</sup> are presented in Fig. 2(a), along with its first derivative (bottom panel). The four peaks in the pristine ScN spectra correspond to Sc  $L_2$  – and  $L_3$  –edges, each split into t<sub>2g</sub> and e<sub>g</sub> levels due to N-octahedral coordination. The peaks I and II correspond to the electronic transition from occupied Sc  $2p_{3/2}$  to unoccupied Sc 3d orbitals, known as Sc  $L_3$ -edge. Similarly, the transition from occupied Sc  $2p_{1/2}$ to unoccupied Sc 3d orbitals is identified as Sc  $L_2$ -edge, as labeled by III and IV. The Sc L-edge and N K-edge absorption spectra overlap, as shown from the ab initio calculation presented as dotted lines [refer to Fig. 2(a)]. The four peak positions for nonimplanted ScN at 399.2 eV (I), 401.7 eV (II), 403.9 eV (III), and 406.2 eV (IV) match well with the earlier report [42]. The spin-orbit coupling splitting energy of Sc 2p, as determined from the separation between either  $t_{2g}$  or  $e_g$  of  $L_3$ - and  $L_2$ -edges, is 4.6 eV, consistent with the core level x-ray photoelectron spectroscopy (XPS) of Sc 2p (see SM Sec. V and Fig. S7(a) for details [51]). The crystal field splitting energy, as obtained from the energy difference between  $t_{2g}$ and  $e_g$  peaks of Sc L-edge, is 2.4 eV, in close agreement with the *ab initio* value of  $\sim$ 2.0 eV, calculated from FMS theory. These values are consistent with the previous literature report [42].

However, C-implantation distorts the N-octahedral geometry and local structure, leading to the further splitting of individual  $t_{2g}$  and  $e_g$  degenerate levels, causing asymmetric broadening and shouldering in the SXAS peaks with a slight shift of the peak positions due to the change in local bonding environment of Sc (see SM Sec. IV for details [51]). The shoulder in peaks II and IV [marked by an asterisk in Fig. 2(a)] indicates a different splitting energy due to the distortion of the octahedra in the presence of carbon. These shoulders are visible even in the first derivative plot, suggesting distortion in the Sc octahedra caused by some N substitution with the implanted C.

With substitutional carbon hole doping (C<sub>N</sub>), the Fermi level is expected to move towards the valence band edge, probed by synchrotron radiation ultraviolet photoelectron spectroscopy (SR-UPS) [guided by the arrow in Fig. 2(b)]. The valence band edge is at ∼1.08 eV below the Fermi level for intentionally undoped ScN and changed to ~0.85 eV for the C-implanted sample with implantation dosage  $\sim$  $5 \times 10^{15}$  cm<sup>-2</sup>. This further indicates the hole-doping nature of implanted carbon in ScN, shifting the Fermi level from the conduction band to the bandgap and leading to carrier compensation upon C-implantation, as observed from the transport measurements. The observed shift in the Fermi level with increasing implantation dosage is consistent with the decrease in electron concentration as calculated theoretically in previous literature reports [81]. The valence band edge of ScN is composed mainly of N 2p characters, slightly hybridized with the Sc 3d states determined from the DFT calculated DOS and PDOS, as shown in the bottom panel of Fig. 2(b). The peak at binding energy  $\sim$ 5.8 eV corresponds to the O 2pstates, showing a large photoionization cross section, which broadens the experimental valence band compared to the DFT calculated DOS. The thermal and instrumental broadening have not been considered in the DFT calculation.

The incorporation of carbon in the nitrogen site is also evident from the XPS depth profile measurements (refer to Appendix A). The C-implanted film (implantation dosage  $\sim 1 \times 10^{15}$  cm<sup>-2</sup>) is sputtered with a 1 keV Ar<sup>+</sup> beam to study the depth profile of carbon inside the sample. The depth profile data shows that without etching, a high concentration of carbon with C 1s peak at  $\sim$ 284.6 eV is observed on the sample surface due to both ion-implantation and the adventitious carbon from postgrowth exposure to the ambient. The main C 1s peak gradually shifts to lower binding energy with reduced intensities representing the implantation-induced C inside the film bonded with metal Sc (refer to Fig. 7(b) in Appendix A). Such a Sc-C bond indicates that C occupies the N site and behaves like a hole dopant, reducing the background electron concentration of pristine ScN. The XPS peak profile of Sc 2p, N 1s, O 1s, and C 1s, along with the detailed discussion, is presented in the SM Sec. V [51]. However, due to the unavoidable carbon contamination, detailed quantification of carbon content is complicated in this case. Furthermore, dielectric spectra obtained from the ellipsometry data fitting reveal an epsilon-near-zero (ENZ) shift from the near- to mid-IR region with increasing carbon implantation, indicating carrier compensation upon carbon implantation (details in Appendix B).

## C. Structural characterization

The structural changes due to C-implantation are further analyzed using high-resolution x-ray diffraction (HRXRD), as shown in Fig. 3(a). Symmetric  $2\theta$ - $\omega$  x-ray diffraction shows that the as-deposited ScN film grows with a single (002) orientation on a single crystalline (001) MgO substrate. The experimental out-of-plane lattice constant of 4.50 Å is obtained from the (002) peak of intentionally undoped ScN. With increasing implantation dosage, the ScN (002) peak shifts to lower  $2\theta$  gradually, indicating out-of-plane lattice expansion (see Fig. 3(a) and SM Table S3 [51]). The slightly higher atomic radius of carbon (70 pm) in comparison to nitrogen (65 pm) [82] and the presence of some interstitial carbon atoms presumably results in this slight lattice expansion (see SM Sec. VII [51]). However, the  $2\theta$  peak also broadens with a shoulder at lower  $2\theta$ , indicating the degradation of crystal quality upon C-implantation [see SM Sec. VIII [51] (see also Ref. [83] therein)]. This is further validated by the full width at half maxima (FWHM) of the rocking curve ( $\omega$ -scan) of the (002) plane, which increases to 1.65° under the highest C-implantation dosage of  $5 \times 10^{16} \, \text{cm}^{-2}$  as compared to the pristine value of 0.93°. The broadness could be related to the tilting of planes due to local distortion from the vacancy clustering caused by the ion-implantation.

The reciprocal space mapping (RSM) of the asymmetric (113) plane for both pristine and implanted samples are shown for comparison in Fig. 3(b) and Fig. 3(c), respectively. The (113) RSM diffraction spot for the implanted sample with a dosage  $\sim 1 \times 10^{15} \, \text{cm}^{-2}$  shows lower peak intensity and higher broadness [refer to Fig. 3(c)], suggesting the degradation of the crystalline quality upon carbon implantation. The obtained in-plane and out-of-plane lattice parameters for pristine ScN comes to be 4.50 Å. Although the in-plane lattice constant for the implanted sample is 4.49 Å, similar to that of bulk, the out-of-plane lattice parameter shows a significant increase with a value of 4.56 Å, indicating the out-of-plane lattice expansion due to the carbon implantation. This is further consistent with the DFT calculated in-plane and out-of-plane lattice constants of the C-implanted ScN, with some of the carbon sitting in the interstitial position with an increase of the out-of-plane lattice constant (refer to Table S6 in the SM [51]). The epitaxial nature of C-implanted ScN is further corroborated by the pole figure measurement of the asymmetric (111) plane, which shows four equally spaced peaks at a 55.45° χ angle, suggesting cubic symmetry [see Fig. 3(d)].

The cross-sectional high-resolution (scanning) transmission electron microscopy (HR(S)/TEM) imaging confirms cubic epitaxial growth of ScN on MgO substrate with an epitaxial relationship of (001) [001] ScN  $\parallel$  (001) [001] MgO [see Fig. 3(e)]. The selected area electron diffraction (SAED) pattern in the inset of Fig. 3(e) demonstrates the local cubic epitaxial nature even when the film is implanted with a dosage of  $5 \times 10^{15}$  cm<sup>-2</sup>. The ScN/MgO interface region shows little waviness in some places, probably due to the misfit dislocation from the lattice mismatch or implantation-induced damage of a few layers of MgO from the interface, as shown by marking in Fig. 3(e). This finding agrees with the observed preshoulder peak in (002) MgO in HRXRD (see Fig. S9(a) in SM [51]). The low magnification high-angle

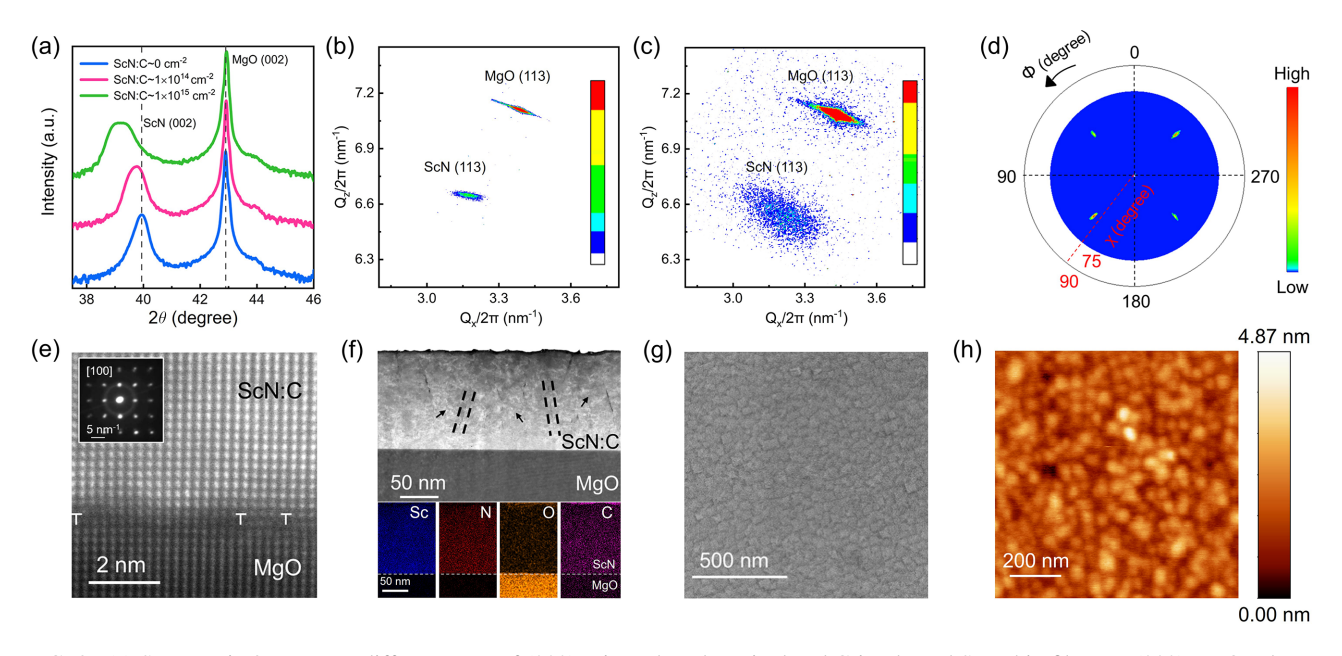


FIG. 3. (a) Symmetric  $2\theta$ - $\omega$  x-ray diffractogram of (002) oriented as-deposited and C-implanted ScN thin films on (002) MgO substrates. The shift of the (002) peak to a lower  $2\theta$  indicates the lattice expansion with increasing carbon implantation dosage. The reciprocal space mapping (RSM) of the asymmetric (113) plane of (b) pristine ScN and (c) carbon-implanted ScN with an implantation dosage of  $\sim$ 1 ×  $10^{15}$  cm<sup>-2</sup>. The reduction of the film peak intensity, as well as an increase in spread, indicates the degradation of the crystallinity on carbon implantation. (d) The pole figure of the asymmetric (111) plane of C-implanted ScN shows four equally spaced diffraction spots, indicating the four-fold symmetric nature, highlighting the epitaxy of the film. (e) The atomic resolution cross-sectional HAADF-STEM imaging of C-implanted ScN represents the coherent [001] growth of ScN on MgO substrate. The inset shows the selective area electron diffraction (SAED) pattern along the [100] zone axis of ScN, further confirming the epitaxial growth on MgO. (f) The HAADF-STEM image depicts the presence of misfit dislocations originating near the ScN-MgO interface and voids separating the grains of the same orientation. The EDS elemental mapping of C-implanted ScN film reveals the uniform distribution of Sc, N, O, and C. (g) FESEM image reveals the square-shaped grains with an average grain size of  $\sim$ 60 nm for the C-implanted sample. The sample morphology remains smooth and compact even after implantation. (h) The AFM image of C-implanted ScN shows an average root-mean-square (RMS) roughness of  $\sim$ 0.63 nm, slightly increased compared to the pristine sample.

annular dark field scanning transmission electron microscopy (HAADF-STEM) reveals the presence of a few voids and extended defects, such as dislocations in the C-implanted film marked by arrows in Fig. 3(f). The HRSTEM-energy dispersive x-ray spectroscopy (EDS) elemental mapping shows a uniform distribution of Sc, C, and N throughout the film, along with unintentional oxygen impurities whose concentration is higher near the surface and reduced inside the film. Although the exact quantification of carbon is difficult due to the presence of adventitious C in the pristine film, a comparison of EDS results shows the presence of  $\sim 2\% - 3\%$  higher atomic percentage of carbon in the implanted film than the pristine one. Plan-view field emission scanning electron microscopy (FESEM) imaging shows no significant damage to ScN film surfaces due to C-implantation. A representative image with an implantation dosage of  $\sim 1 \times 10^{15}$  cm<sup>-2</sup> presented in Fig. 3(g) reveals a cubic grain of average size  $\sim 60$  nm with grain boundaries forming a smooth surface. Atomic force microscopy (AFM) imaging [see Fig. 3(h)] reveals an average RMS surface roughness of  $\sim$ 0.63 nm for the C-implanted film that is slightly higher than the surface roughness of the good quality pristine ScN of 0.31 nm as reported earlier [20].

## D. Formation energy and DOS from first-principles DFT

The first-principles DFT calculations are further employed to understand the formation energies and energy levels of carbon-related substitutional and defect complexes in ScN. The calculations are performed using the DFT+U approach to account for the DFT bandgap underestimation. The calculated  $\Gamma$  – X indirect bandgap of pristine ScN is 0.80 eV [refer to Fig. 4(a)], consistent with previous studies [84,85]. The valence band of pristine ScN consists of predominantly N 2p states, and the conduction band mainly of the Sc 3d characters, indicating an optical transition between N 2p to Sc 3d electronic states [see Fig. 4(a)]. As-deposited ScN under N-rich growth conditions shows an n-type degenerate electronic transport due to the presence of substitutional oxygen (O<sub>N</sub>) impurities and possible N-vacancies, which act as donors in ScN [Fig. 4(b)]. Unlike N-vacancy,  $V_{Sc}$  shifts the Fermi level inside the valence band, suggesting a p-type electronic transport.

Previous studies show that the formation of N vacancy is more favorable than Sc-vacancy ( $V_{Sc}$ ) based on thermodynamic formation energy calculations [45,86]. However, the formation of complex defects with  $V_{Sc}$  and a nearest substitutional oxygen ( $O_N$ ) is energetically more favorable than the single Sc-vacancy. This complex defect behaves as p-type dopants with the position of the Fermi level inside the valence band [see Fig. 4(c)], reducing the excess electron concentration in ScN. The presence of small oxygen impurities in ScN is also evident from the formation enthalpy ( $\Delta H^f$ ) of ScN and Sc<sub>2</sub>O<sub>3</sub>. The calculated  $\Delta H^f$  of ScN and Sc<sub>2</sub>O<sub>3</sub> are

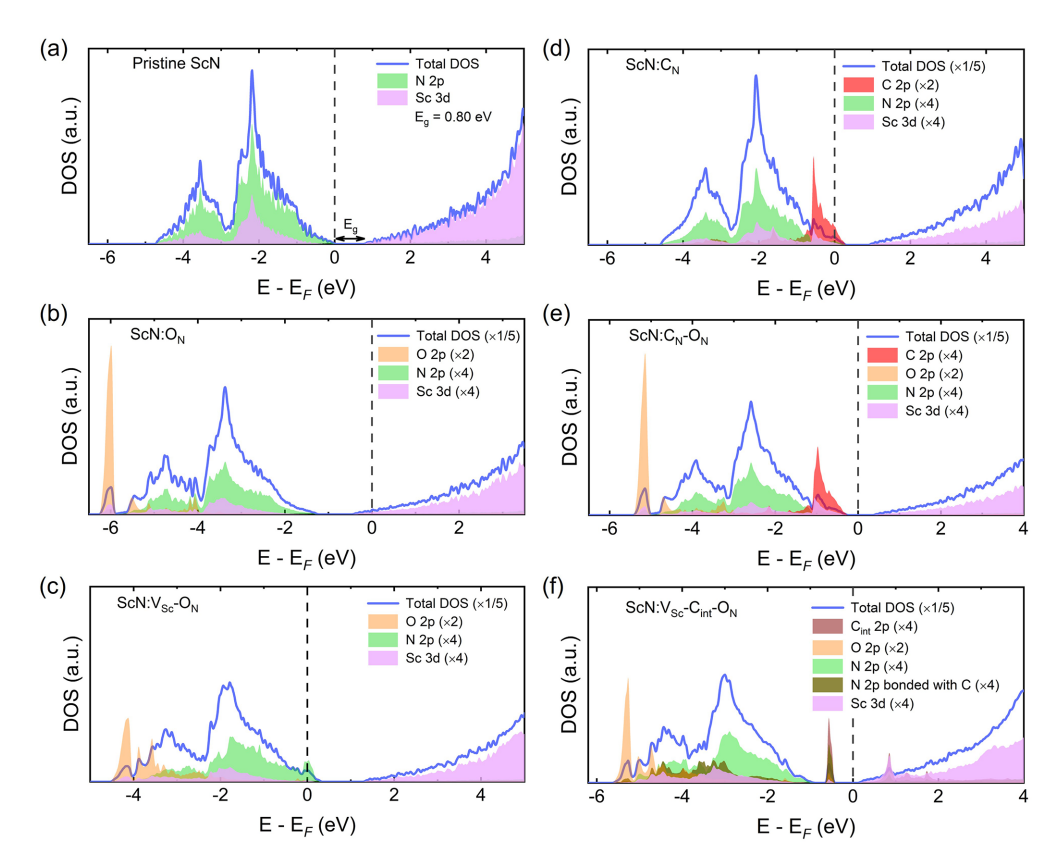


FIG. 4. Total and partial electronic density of states for pristine and C-doped ScN with various defect configurations. (a) pristine ScN, (b) O-substitution in N-site  $(O_N)$  as n-type dopant, (c) vacancy of Sc and O-substitution in the nearest N-site forms a p-type complex defect, (d) C-substitution in N-site  $(C_N)$  as p-type dopant, (e) C-substitution in N-site and O-substitution in the nearest N-site, forming defect complex with effective shifts of the Fermi level into the bandgap compared to the O-substitution in N-site defect, indicating the carrier compensation, (f) vacancy of Sc, C-interstitial, and O-substitution in N-site forms an n-type complex defect. The Fermi energy is set to 0 eV for each case.

-3.91 and -19.63 eV/fu, respectively, as obtained from GGA calculations using QE, and -4.24 and -18.81 eV/fu from HSE06 hybrid functional calculations using VASP. The higher formation enthalpy of  $Sc_2O_3$  indicates the presence of small unavoidable oxygen impurities in the Sc-target used in the sputtering. The electronic density of states shows a peak of O 2p states at  $\sim$ -5 eV from the valence band edge [see Fig. 4(b)], which is also prominent in the experimental UPS data, as shown in Fig. 2(b). The compensation of such excess electron concentration requires effective hole dopants, and carbon appears to be a suitable choice as it contains one less electron compared to N.

The incorporation of substitutional C in the N site  $(C_N)$  shifts the Fermi level inside the valence band at about  $\sim 0.3$  eV for  $\sim 3.1\%$  C-doped ScN  $(ScN_{0.969}C_{0.031})$ , indicating an acceptor-type dopant in ScN [refer to Fig. 4(d)]. The C 2p states are located at the valence band edge, as shown in Fig. 4(d), indicating small activation for the electronic transport (see Fig. S2(c) in SM [51]). However, such feature is not prominent in the experimental SR-UPS data as the C 2p atomic subshell has the lowest photoionization cross section value among the others [see SM Sec. XII and Table S7 [51] (see also Ref. [87] therein)], and the amount of C present in the ScN is low,  $\sim 2.0\% - 3.0\%$ , as compared to the Sc, N, and unintentional O impurity. The effect of C as a hole dopant  $(C_N)$  can only be verified experimentally from the decreasing carrier concentration with increasing C-implantation

dosage in the carrier concentration vs temperature plot, as shown in SM Sec. III and Fig. S2(a) [51]. The total density of states further reveals the rigid band electronic nature of ScN, even with the substitutional carbon. Furthermore, the Fermi level for defect complex  $C_N$ – $O_N$  is located inside the bandgap [see Fig. 4(e)], indicating electron compensation with C-implantation over the presence of a small oxygen impurity in ScN. This further correlates with the experimental observation of electron compensation in ScN with moderate C-implantation dosage, a significant number of C atoms occupy implantation-induced N-vacancy sites and behave like a hole dopant.

The calculated formation energy of a single neutral carbon interstitial ( $C_{\rm int}$ ) defect is positive and relatively high ( $\sim$ 9.37 eV), making it unlikely to form easily. However, defect complexes associated with  $C_{\rm int}$ ,  $V_{\rm Sc}$ , and  $O_{\rm N}$  can form due to their lower formation energy. The projected density of states for  $V_{\rm Sc}-C_{\rm int}-O_{\rm N}$  reveals the presence of defect states inside the bandgap, having a hybridized orbital character from interstitial C 2p and N 2p bonded with  $C_{\rm int}$ , along with an n-type electronic nature with the Fermi level close to the conduction band edge, as shown in Fig. 4(f). These midband gap defect states cause the Fermi level pinning within the bandgap, reduce the mobility and increase the resistivity of the C-implanted films, as observed experimentally.

The DFT-obtained both in-plane and out-of-plane lattice parameters for possible single and complex defects are listed

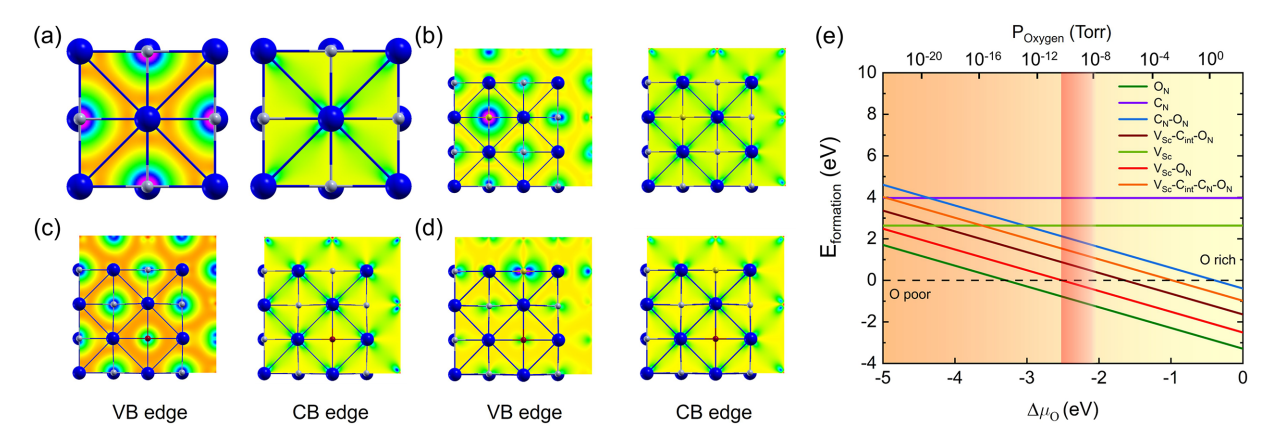


FIG. 5. The integrated charge densities of VBM-100 meV and CBM+100 meV for (a) pristine ScN, (b) C-substitution in N-site, (c) O-substitution in N-site, and (d) C-substitution in N-site and O-substitution in the nearest N-site. (e) Calculated defect formation energy of several individual defects and defect complexes as a function of oxygen chemical potential and oxygen partial pressure. The shaded region corresponds to the background oxygen partial pressure inside the sputtering chamber.

in Table S6 in the SM [51]. The DFT+U optimized lattice parameter of pristine ScN is 4.56 Å, higher than the experimental values due to the Hubbard-U correction. The in-plane and out-of-plane lattice constants remain unchanged for most of the single and complex defects, except those with interstitial carbon (V<sub>Sc</sub>-C<sub>int</sub>-O<sub>N</sub>). The in-plane lattice constant of V<sub>Sc</sub>-C<sub>int</sub>-O<sub>N</sub> is similar to the pristine value, but the out-of-plane lattice constant increases by  $\sim 0.66\%$ , consistent with the experimental increase of the out-of-plane lattice constant with C-implantation, although the percentile increment in the experiment is higher than the calculated value. This reveals that some of the implanted carbon goes to the interstitial sites, forming complex defects with implantation-induced Sc-vacancy and substitutional oxygen, with the out-of-plane lattice expansion. However, a major amount of implanted carbon goes into the implantation-created N-vacancy sites as substitutional carbon (C<sub>N</sub>), responsible for the carrier compensation in the implanted films.

Charge densities integrated for 100 meV away from both the valence and conduction band edges correspond to the N 2p and Sc 3d orbitals, respectively, for pristine and carbondoped ScN with various defect configurations [see Figs. 5(a) to 5(d)]. However, extra C 2p states are in the valence band edge only for the substitutional carbon (C<sub>N</sub>) defects, as shown in Figs. 5(b) and 5(d). The calculated neutral defect formation energies as a function of oxygen chemical potential and partial pressure indicate the possibility of the formation of individual defects and defect complexes. Among all possible defects, O<sub>N</sub> is the most stable defect with higher negative formation energies above the oxygen partial pressure of 10<sup>-12</sup> Torr [refer to Fig. 5(e)]. The formation energy of  $C_N$  is positive and consistent with the previous literature report, indicating the inability to form spontaneously [45]. However, the formation energy of p-type defect complex  $C_N - O_N$  is lower than  $C_N$  but still positive, suggesting this type of complex defect can be formed in a nonequilibrium process such as ion-implantation. Even a single Sc vacancy defect has also higher formation energy and is unable to form, but its p-type defect complex V<sub>Sc</sub>-O<sub>N</sub> has a much lower formation energy and is easy to form. Even interstitial carbon-related *n*-type complex defects, such as  $V_{Sc}-C_{int}-O_N$  and  $V_{Sc}-C_{int}-C_N-O_N$  in their neutral state, have negative formation energies in the higher oxygen partial pressure region, as shown in Fig. 5(e).

However, the neutral defect formation energies alone are insufficient to determine the correct formation energies quantitatively. Therefore, charged defect formation energies as a function of the Fermi level position are essential to fully understand the defect physics in ScN. The calculated formation energies of various charged defects as a function of the Fermi level position are shown in Fig. 6. The slope of each straight line corresponds to the defect charge. Although the defect formation energy of neutral carbon in the interstitial site (C<sub>int</sub>) is quite high, the charged defect counterparts have lower formation energies as a function of the Fermi level. The defect formation energy of  $C_{int}^{+4}$  at the VBM is 2.21 eV [see Fig. 6(a)], which is substantially lower than the formation energy of neutral C<sub>int</sub>, suggesting the possibility of C to go into the interstitial tetrahedral voids with +4 charge state and average C-N bond length of 1.58 Å (see Fig. S13(a) in SM [51]), yielding a donor-type doping signature in ScN. The thermodynamic transition level (+4/+3) occurs at 0.25 eV below the CBM as shown in Fig. 6(a).

The charged defect formation energies of Cint in ScN are quite similar to Cint defects in GaN, as reported in previous literature [46,88]. Additionally, defect formation energy calculations reveal that clustering of such interstitial C, along with the cation (Sc) vacancy and oxygen substitution in the N-site (O<sub>N</sub>) in +2 charge state, further lowers the formation energy as compared to the  $C_{int}^{+4}$  point defect, suggesting its formation as a charged defect complex in ScN. Depending on the relative position of Cint and ON, two different configurations of the same defect complex, V<sub>Sc</sub>-C<sub>int</sub>-O<sub>N</sub>, can form, as shown in Figs. S13(b) and S13(c) in the SM [51]. Among them, one has the lowest formation energy, named  $V_{Sc}-C_{int}-O_{N}$  (1), as shown in Fig. 6(a). The defect formation energy of another complex defect,  $V_{Sc}-C_{int}-C_{N}-O_{N}$ , with +1 charge state, is quite high in the N-rich condition [see Fig. 6(a)].

The formation energy of  $C_N$  at N-rich conditions is also high, with a thermodynamic transition level (0/-1) near the VBM. However, its defect complex,  $C_N - O_N$ , has lower formation energy, indicating the stability of  $C_N$  with the presence

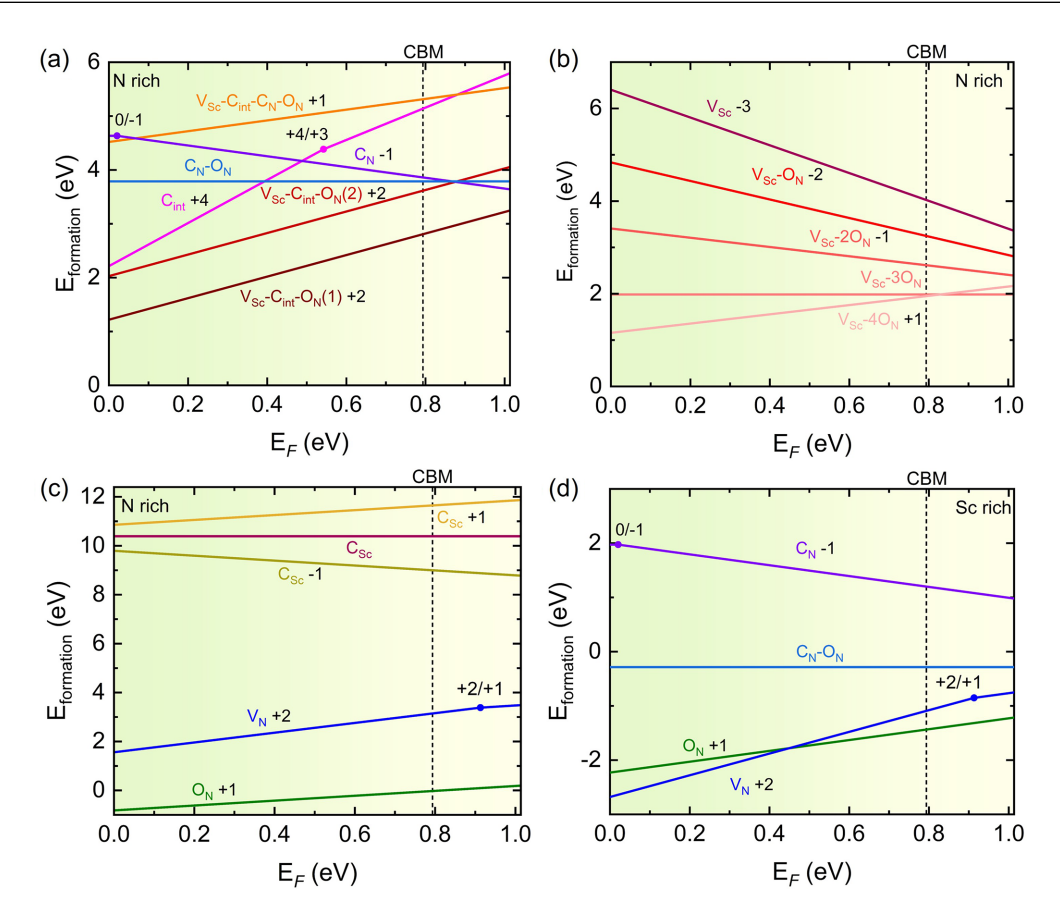


FIG. 6. Thermodynamic formation energy of native defects and defect complexes in ScN under both N-rich and Sc-rich conditions as a function of the Fermi level. The VBM is set at zero energy, and the Fermi level varies throughout the bandgap. The CBM is marked by the dashed line. (a) Formation energy of C-related point defects such as  $C_N$ ,  $C_{int}$ , along with their defect complexes with other point defects, like  $V_{Sc}$ ,  $O_N$ , in the N-rich condition. (b) Formation energy of  $V_{Sc}$  and  $V_{Sc}$ – $nO_N$  complex defects in the N-rich case. (c) Formation energy of  $C_{Sc}$  in different charge states and  $V_N$  and  $O_N$  with charged states +2 and +1, respectively, in the N-rich condition. (d) Formation energy of  $C_N$ ,  $C_N$ – $O_N$ ,  $V_N$ , and  $O_N$  under the Sc-rich condition with their suitable charge states. Charges of each point defect and defect complexes are mentioned.

of oxygen atoms in the neighboring N-site [refer to Fig. 6(a)]. Similarly,  $V_{Sc}$  in -3 charge state has higher formation energy, but its defect complexes V<sub>Sc</sub>-nO<sub>N</sub>, with lower formation energy, can be formed as shown in Fig. 6(b), consistent with the previous report [50]. The formation energies of acceptortype defects  $V_{Sc}$ - $O_N$  with -2 charge state and  $V_{Sc}$ - $2O_N$ with -1 charge state are lower than that of the donor-type V<sub>Sc</sub>-C<sub>int</sub>-O<sub>N</sub> with +2 charge state at a position of the Fermi level corresponding to a carrier concentration of ~  $4-5\times10^{20}\,\mathrm{cm}^{-3}$ . Meanwhile, C-related acceptors like  $C_{\rm N}$ with -1 charge state and the neutral  $C_N - O_N$  complex have slightly higher formation energies ( $\sim 0.40 - 0.54$  eV) than V<sub>Sc</sub>-C<sub>int</sub>-O<sub>N</sub> (refer to Fig. 9 in Appendix C). Such complexes form easily due to the Coulomb attraction between positively charged donors (O<sub>N</sub>) and negatively charged acceptors (C<sub>N</sub>, V<sub>Sc</sub>), leading to the electron compensation in ScN with the Fermi level moving away from the CBM [see Fig. 4(c) and Fig. 4(e)].

The C substitutional point defect in the Sc-site  $(C_{Sc})$  is also unlikely to form due to the quite high formation energy in various charge states, as shown in Fig. 6(c). The most stable point defect in ScN is  $O_N^+$ , having a shallow donor nature in both the N-rich and Sc-rich conditions [see Fig. 6(c) and

Fig. 6(d)], consistent with the previous reports [45,50]. The nitrogen-vacancy  $(V_N)$  acts as a donor in ScN with positive formation energy in the N-rich condition, as shown in Fig. 6(c). However, the formation energy of  $V_N^{+2}$  is negative at the entire Fermi level position inside the bandgap for the Sc-rich condition and contributes electrons to the conduction band [see Fig. 6(d)], in agreement with the previous reports [11,45]. In the Sc-rich condition, both  $C_N$  and  $C_N - O_N$  have significantly lower formation energies as compared to the N-rich condition, suggesting the improved hole-doping ability of  $C_N$  as shown in Fig. 6(d). However, the ScN thin film deposited at Sc-rich conditions contains a significant amount of N-vacancy donor defects, suggesting further difficulty in carrier compensation using C doping through cosputtering.

The analysis of both the neutral, charged defects and defect complexes qualitatively explains the experimentally observed electron compensation in the C-implanted ScN thin films deposited under N-rich growth conditions. The incorporation of carbon inside ScN under N-rich conditions through cosputering did not result in any electron compensation due to the formation of a stable  $V_{\text{Sc}}-C_{\text{int}}-O_{\text{N}}$  donor-type defect complex [see Table S1 and Fig. 6(a)]. To overcome this challenge, we have used the room-temperature ion-implantation

method, which is inherently a nonequilibrium method, where implanted C creates both N and Sc vacancies, and the next implanted carbon atoms occupy the N vacancy sites in such a nonequilibrium process and also form  $C_N - O_N$  defect complex, leaving aside Sc-vacancies due to the very high formation energy of  $C_{Sc}$  [see Fig. 6(c)].

The comparison between DOS shows that with respect to the pristine ScN:O<sub>N</sub>, where the Fermi level is situated inside the conduction band, the formation of both C<sub>N</sub> and C<sub>N</sub>-O<sub>N</sub> complex defects lead to the shift of the Fermi level towards the valence band [see Fig. 4(b), Fig. 4(d), and Fig. 4(e)], suggesting carrier compensation under the formation of the C<sub>N</sub> and C<sub>N</sub>-O<sub>N</sub> defect complex in the C-implanted ScN thin films without annealing. However, implantation-induced Sc-vacancy along with neighboring O<sub>N</sub>'s (V<sub>Sc</sub>-O<sub>N</sub> and V<sub>Sc</sub>-2O<sub>N</sub>), having lower formation energies than V<sub>Sc</sub>-C<sub>int</sub>-O<sub>N</sub> for the position of the Fermi level inside the conduction band (see Fig. 9 in Appendix C), are also responsible for carrier compensation, as the Fermi level for V<sub>Sc</sub>-O<sub>N</sub> defect complex shifts towards the valence band as compared to the O<sub>N</sub> point defect from the DOS calculations, as shown in Fig. 4(c). However, at the higher implantation dosage, the compensation effect is suppressed due to the occupation of excess C in the interstitial sites and forming donor-type defect complex  $V_{Sc}-C_{int}-O_N$  with +2 charge state that counteract the C<sub>N</sub>'s acceptor doping ability and lead to a saturation in the carrier concentration. Therefore, our theoretical calculations support the experimentally observed acceptor nature of C under the moderate ion-implantation dosage. It also explains the saturation in the acceptor doping ability as well as the amphoteric nature of implanted C in ScN at higher implantation dosage, and also the inability to achieve any acceptor doping with magnetron cosputtering.

Furthermore, on annealing, the system tends to lower its energy by substitutional carbon ( $C_N$ ) going into the more stable and equilibrium interstitial positions, forming isolated nitrogen vacancies and the defect complex with neighboring  $V_{Sc}$  and oxygen in the nitrogen site ( $V_{Sc}-C_{int}-O_N$ ), which is thermodynamically more stable than individual  $C_N$  from the equilibrium formation energy analysis, reducing the hole doping ability of C in ScN. However, mobility does not improve due to the higher impurity scattering from the excess donor defect  $V_{Sc}-C_{int}-O_N$  in its +2 charge state. (see SM Sec. X [51]). This also explains the unsuccessful attempt to observe the carrier compensation and hole-doping nature of carbon during cosputtering methods, where most of the doped carbon went to the interstitial positions and formed n-type defect complexes.

## IV. CONCLUSION

In conclusion, this work experimentally explores the feasibility of carbon doping in ScN. Despite the higher formation energy, acceptor-type  $C_N$  and acceptor complex defects  $C_N - O_N$ ,  $V_{Sc} - O_N$ , and  $V_{Sc} - 2O_N$  can be formed by employing the ion-implantation method that enables the formation of nonequilibrium defects. The formation of anion-substituted  $C_N$  in ScN is evident from the decrease in the electron concentration by more than one order for a C implantation dosage of  $5 \times 10^{16} \, \mathrm{cm}^{-2}$ . The Sc-C bond formation, resultant distortion,

and lowering of the Fermi level towards the valence band edge are apparent from XPS, XAS, and UPS measurements. The C-implanted ScN films with compensated electrons preserve crystallinity and elemental homogeneity. Additionally, the first-principles calculations of both neutral and charged defect formation energies revealed the formation of acceptor-type defect complexes such as  $C_N-O_N$ ,  $V_{Sc}-O_N$ , and  $V_{Sc}-2O_N$ , which explain the experimental carrier compensation in ScN on carbon ion-implantation. However, at higher implantation dosage, the compensation effect is suppressed due to the formation of a stable V<sub>Sc</sub>-C<sub>int</sub>-O<sub>N</sub> n-type defect complex. With such detailed experimental and theoretical analysis, this work addresses the challenges associated with carbon doping in ScN, while also offering alternative approaches for doping and enabling precise tuning of carrier concentration and thereby associated material properties.

### ACKNOWLEDGMENTS

S.R., D.R., S.K.M., and B.S. acknowledge the International Centre for Materials Science (ICMS), Sheikh Sagr Laboratory (SSL), and SAMat research facilities in JNCASR for support during this project. B.S. acknowledges the Anusandhan National Research Foundation (ANRF) in India for a Core Research Grant No. CRG/2023/007061 for financial support. S.R. and P.D. thank the Council of Scientific & Industrial Research (CSIR) for the fellowship. D.R., S.K.M., A.D., R.K., S.M., and B.Y. thank JNCASR for the fellowship. S.R. and B.S. sincerely acknowledge the support and resources provided by PARAM Yukti Facility under the National Supercomputing Mission (NSM), Government of India, at the Jawaharlal Nehru Centre for Advanced Scientific Research (JNCASR), Bangalore. S.R. acknowledges Dr. Sanjay Nayak from Silicon Austria Labs GmbH, Mr. Ravid Mojumder from Pennsylvania State University, USA, and Dr. Bidesh Biswas from JNCASR, Bangalore, for helpful discussions regarding the theoretical modeling of XAS, charged defect formation energy calculation, and XPS fittings. M.G. and A.I.K.P. acknowledge the facilities of Sydney Microscopy and Microanalysis at the University of Sydney. M.B. thanks Shri. Suvankar Paul for his help during the UPS measurement at BL-10, Indus-2. The authors greatly acknowledge Professor Giridhar U. Kulkarni (JNCASR, Bangalore) for the helpful discussion and comments.

S.R., D.R., and B.S. conceived this project. D.R. and S.K.M. deposited thin films. D.R. and S.K.M. performed the electrical measurements. S.S. performed the C-ion (C<sup>-</sup>) implantation in thin films. S.R. and B.S. performed the theoretical modeling and analysis of the results. A.D., R.K., and S.M. performed the structural characterization. M.G. from UGC-DAE performed the XAS measurement. P.D. performed the optical measurements. A.I.K.P. performed the TEM sample preparation, and M.G. from the University of Sydney performed the TEM imaging and EDS mapping. B.Y. performed the AFM imaging. M.B. performed the Synchrotron UPS measurement under the assistance of T.G. All authors discussed and contributed to the preparation of the manuscript.

The authors have no conflict of interest.

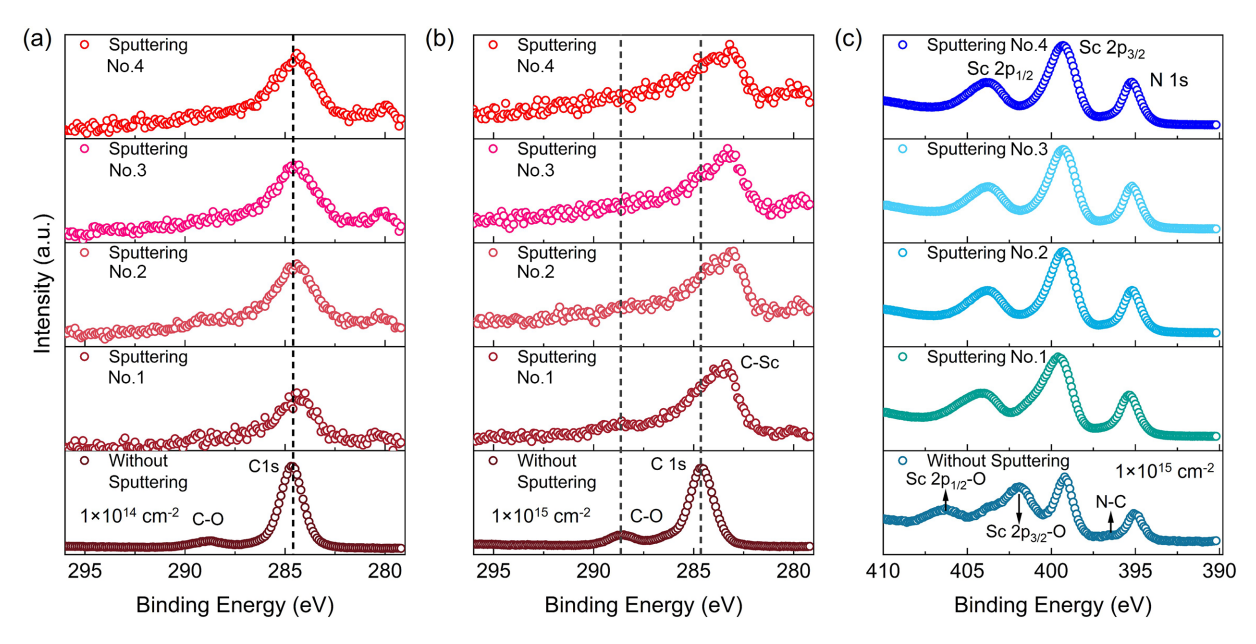


FIG. 7. (a) Depth profile of C *Is* XPS peak of ScN:  $C \sim 1 \times 10^{14}$  cm<sup>-2</sup> film. Without sputtering, the C *Is* peak is located at 284.6 eV, corresponding to an adventitious carbon on the sample surface, and the C *Is* peak position remains unchanged with sputtering. (b) C *Is* depth profile of ScN thin film with an implantation dosage of  $1 \times 10^{15}$  cm<sup>-2</sup>. The binding energy of the C *Is* peak shifts to the lower energy side from the adventitious carbon position with sputtering, indicating the formation of Sc-C bonds within the sample. (c) Depth profile of Sc *2p* and N *Is* XPS peaks in ScN:  $C \sim 1 \times 10^{15}$  cm<sup>-2</sup> film. The sample surface shows strong oxygen contamination from strong Sc-O bonding, which eventually reduces inside the sample with sputtering.

## DATA AVAILABILITY

The data that support the findings of this article are not publicly available. The data are available from the authors upon reasonable request.

# APPENDIX A: X-RAY PHOTOELECTRON SPECTROSCOPY DEPTH PROFILE ANALYSIS

The depth profile of the core-level electronic structure is determined from XPS measurements by observing C *Is*, Sc *2p*, and N *Is* peaks, as shown in Fig. 7. The XPS peaks are calibrated with respect to the adventitious C *Is* peak at 284.6 eV present in the sample surface without sputtering, as mentioned in the previous study [89]. The C *Is* peak position remains

unchanged with sputtering for lower dosages [Fig. 7(a)] but shifts to the lower energy side for higher C-implanted samples [Fig. 7(b)] indicating the formation of Sc-C bonds with increasing C-implantation dosage, where C goes into the N site, observing an effective carrier compensation. As Sc is more prone to oxidation, a strong Sc-O peak is observed at the sample surface, which eventually fades within the sample, as evident in the Sc 2p XPS peak with sputtering. The ScN feature is more prominent, as shown in Fig. 7(c).

## APPENDIX B: SPECTROSCOPIC ELLIPSOMETRY MEASUREMENT

The compensation of electron concentration in C-implanted ScN is verified further by analyzing its optical

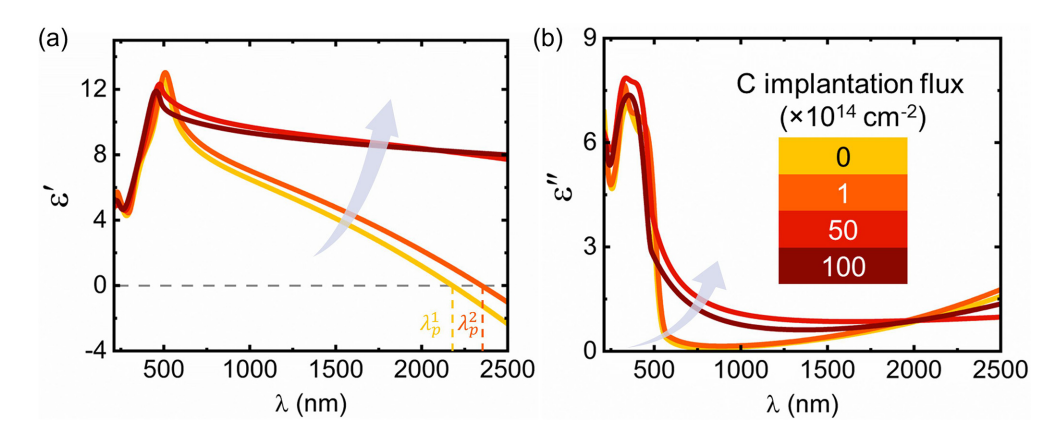


FIG. 8. (a) Real  $(\varepsilon_1)$  and (b) imaginary  $(\varepsilon_2)$  parts of the dielectric permittivity of pristine and C-implanted ScN thin films from ellipsometry data fitting. The plasmonic response shifts from short-wavelength IR (SWIR) to the long-wavelength region with increasing implantation dosage due to the compensation of carrier concentration from carbon in the nitrogen site  $(C_N)$ .

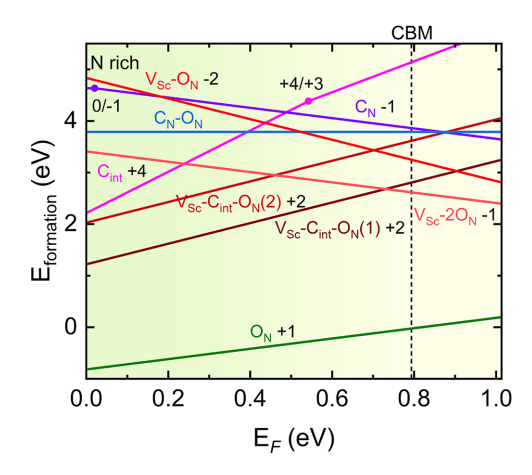


FIG. 9. Formation energy of major point defects  $O_N$ ,  $C_N$ , and  $C_{int}$  and defect complexes  $V_{Sc} - O_N$ ,  $V_{Sc} - 2O_N$ , and  $V_{Sc} - C_{int} - O_N$  under N-rich conditions as a function of the Fermi level position, showing in a single plot. The VBM is set at zero energy, and the Fermi level varies throughout the bandgap. The CBM is marked by the dashed line.

properties. The dielectric permittivity is derived from the fitting of the experimental Psi  $(\Psi)$  and Delta  $(\Delta)$  spectra using variable-angle spectroscopic ellipsometry. For pristine ScN, the real part of the permittivity  $(\varepsilon')$  exhibits a crossover from positive to negative values, indicating an epsilon-near-zero (ENZ) transition, around 2177 nm, characteristic of plasmonic behavior  $(\lambda_n^1)$  as shown in Fig. 8(a).

Under the C-implantation into ScN, the ENZ crossover shifts to longer wavelengths, correlating with a reduction in electron concentration. In highly C-implanted ScN samples,  $\varepsilon'$  remains positive across the entire measured spectral range, indicating a complete transition to dielectric behavior.

Additionally, the imaginary part of the permittivity ( $\varepsilon''$ ), which represents optical losses, is nearly zero below the bandgap in pristine ScN. However, with increased C-implantation, optical losses below the bandgap increase [refer to Fig. 8(b)] due to implantation-induced defects. Interestingly, losses at longer wavelengths, originating from intraband electron transitions and characteristic plasmonic response, diminish with C implantation.

These observations clearly demonstrate that increasing C-implantation reduces carrier concentration, resulting in a progressive transition from short-wavelength infrared (SWIR) plasmonic behavior to a purely dielectric nature in the observed spectral range of the ellipsometer.

# APPENDIX C: THERMODYNAMIC FORMATION ENERGY OF MAJOR POINT DEFECTS AND DEFECT COMPLEXES

The formation energy of major point defects ( $C_N$ ,  $C_{int}$ , and  $O_N$ ) and defect complexes ( $V_{Sc}-O_N$ ,  $V_{Sc}-2O_N$ ,  $C_N-O_N$ , and  $V_{Sc}-C_{int}-O_N$ ) regarding the current scenario of C-implantation in ScN under the N-rich condition is shown as a combined plot in Fig. 9. The Fermi level position is extended inside the conduction band, corresponding to the nonimplanted pristine ScN's electron concentration of  $\sim 5 \times 10^{20}\,\mathrm{cm}^{-3}$ .

<sup>[1]</sup> S. Nakamura, N. Iwasa, M. S. Masayuki Senoh, and T. M. T. Mukai, Hole compensation mechanism of *p*-type GaN films, Jpn. J. Appl. Phys. 31, 1258 (1992).

<sup>[2]</sup> P. Y. Yu and M. Cardona, Fundamentals of Semiconductors, Vol. 28 (Springer, Berlin, Heidelberg, 2010).

<sup>[3]</sup> H. Obloh, K. H. Bachem, U. Kaufmann, M. Kunzer, M. Maier, A. Ramakrishnan, and P. Schlotter, Self-compensation in Mg doped *p*-type GaN grown by MOCVD, J. Cryst. Growth 195, 270 (1998).

<sup>[4]</sup> B. G. Streetman and S. Banerjee, *Solid State Electronic Devices* (Pearson Education, 2014).

<sup>[5]</sup> S. Adachi, Properties of Semiconductor Alloys (Wiley, Chichester, 2009).

<sup>[6]</sup> T. Taliercio and P. Biagioni, Semiconductor infrared plasmonics, Nanophoton. 8, 949 (2019).

<sup>[7]</sup> L. Conrads, L. Schüler, K. G. Wirth, A. Cleri, A. Heßler, L. Jung, M. Wuttig, D. Chigrin, J. P. Maria, and T. Taubner, Real-space imaging of confined infrared surface plasmon polaritons on doped semiconductors covered with phase-change materials, Sci. Adv. 11, eadr6844 (2025).

<sup>[8]</sup> R. Liu, J. Lan, X. Tan, Y. Liu, G. Ren, C. Liu, Z. Zhou, C. Nan, and Y. Lin, Carrier concentration optimization for thermoelectric performance enhancement in *n*-type Bi<sub>2</sub>O<sub>2</sub>Se, J. Eur. Ceram. Soc. 38, 2742 (2018).

<sup>[9]</sup> P.-C. Wei, C.-X. Cai, C.-R. Hsing, C.-M. Wei, S.-H. Yu, H.-J. Wu, C.-L. Chen, D.-H. Wei, D.-L. Nguyen, M. M. C. Chou, and Y.-Y. Chen, Enhancing thermoelectric performance by

Fermi level tuning and thermal conductivity degradation in  $(Ge_{1-x}Bi_x)$ Te crystals, Sci. Rep. 9, 8616 (2019).

<sup>[10]</sup> Y. Oshima, E. G. Villora, and K. Shimamura, Hydride vapor phase epitaxy and characterization of high-quality ScN epilayers, J. Appl. Phys. 115, 153508 (2014).

<sup>[11]</sup> J. S. Cetnar, A. N. Reed, S. C. Badescu, S. Vangala, H. A. Smith, and D. C. Look, Electronic transport in degenerate (100) scandium nitride thin films on magnesium oxide substrates, Appl. Phys. Lett. 113, 192104 (2018).

<sup>[12]</sup> P.-C. Wei, S. Chattopadhyay, M.-D. Yang, S.-C. Tong, J.-L. Shen, C.-Y. Lu, H.-C. Shih, L.-C. Chen, and K.-H. Chen, Room-temperature negative photoconductivity in degenerate InN thin films with a supergap excitation, Phys. Rev. B 81, 045306 (2010).

<sup>[13]</sup> H. Al-Atabi, Q. Zheng, J. S. Cetnar, D. Look, D. G. Cahill, and J. H. Edgar, Properties of bulk scandium nitride crystals grown by physical vapor transport, Appl. Phys. Lett. 116, 132103 (2020).

<sup>[14]</sup> E. Mozafari, B. Alling, P. Steneteg, and I. A. Abrikosov, Role of N defects in paramagnetic CrN at finite temperatures from first principles, Phys. Rev. B 91, 094101 (2015).

<sup>[15]</sup> A. R. Smith, H. A. H. Al-Brithen, D. C. Ingram, and D. Gall, Molecular beam epitaxy control of the structural, optical, and electronic properties of ScN(001), J. Appl. Phys. 90, 1809 (2001).

<sup>[16]</sup> J. More-Chevalier, L. Horákb, S. Cichoňa, P. Hruškaab, J. Čížekb, M. O. Liedkec, M. Butterlingc, A. Wagnerc, J. Bulířa,

- P. Hubíka, Z. Gedeonováa, and J. Lančok, Positron structural analysis of ScN films deposited on MgO substrate, Acta Phys. Pol. A **137**, 209 (2020).
- [17] M. S. Haseman, B. A. Noesges, S. Shields, J. S. Cetnar, A. N. Reed, H. A. Al-Atabi, J. H. Edgar, and L. J. Brillson, Cathodoluminescence and x-ray photoelectron spectroscopy of ScN: Dopant, defects, and band structure, APL Mater. 8, 081103 (2020).
- [18] G. B. Rayner, N. O'Toole, B. Liu, J. Shallenberger, J. Zhu, T. Palacios, P. Behera, S. Cheema, B. Johs, and N. A. Strnad, Ultrahigh purity plasma-enhanced atomic layer deposition and electrical properties of epitaxial scandium nitride, J. Vac. Sci. Technol. A 43, 020401 (2025).
- [19] S. Kerdsongpanya, N. Van Nong, N. Pryds, A. Žukauskaitė, J. Jensen, J. Birch, J. Lu, L. Hultman, G. Wingqvist, and P. Eklund, Anomalously high thermoelectric power factor in epitaxial ScN thin films, Appl. Phys. Lett. 99, 232113 (2011).
- [20] P. V. Burmistrova, J. Maassen, T. Favaloro, B. Saha, S. Salamat, Y. Rui Koh, M. S. Lundstrom, A. Shakouri, and T. D. Sands, Thermoelectric properties of epitaxial ScN films deposited by reactive magnetron sputtering onto MgO(001) substrates, J. Appl. Phys. 113, 153704 (2013).
- [21] S. Kerdsongpanya, B. Alling, and P. Eklund, Effect of point defects on the electronic density of states of ScN studied by first-principles calculations and implications for thermoelectric properties, Phys. Rev. B 86, 195140 (2012).
- [22] K. C. Maurya, D. Rao, S. Acharya, P. Rao, A. I. K. Pillai, S. K. Selvaraja, M. Garbrecht, and B. Saha, Polar semiconducting scandium nitride as an infrared plasmon and phonon-polaritonic material, Nano Lett. 22, 5182 (2022).
- [23] D. Rao, A. I. K. Pillai, M. Garbrecht, and B. Saha, Scandium nitride as a gateway III-nitride semiconductor for both excitatory and inhibitory optoelectronic artificial synaptic devices, Adv. Electron. Mater. 9, 2200975 (2023).
- [24] D. Rao, S. Acharya, and B. Saha, Demonstration of compensated n-type scandium nitride Schottky diodes, J. Phys. D. Appl. Phys. 56, 074004 (2023).
- [25] B. Biswas and B. Saha, Development of semiconducting ScN, Phys. Rev. Mater. **3**, 020301 (2019).
- [26] P. Eklund, S. Kerdsongpanya, and B. Alling, Transition-metalnitride-based thin films as novel energy harvesting materials, J. Mater. Chem. C 4, 3905 (2016).
- [27] M. Garbrecht, J. L. Schroeder, L. Hultman, J. Birch, B. Saha, and T. D. Sands, Microstructural evolution and thermal stability of HfN/ScN, ZrN/ScN, and Hf<sub>0.5</sub>Zr<sub>0.5</sub>N/ScN metal/semiconductor superlattices, J. Mater. Sci. **51**, 8250 (2016).
- [28] P. Das, K. C. Maurya, J. L. Schroeder, M. Garbrecht, and B. Saha, Near-UV-to-near-IR hyperbolic photonic dispersion in epitaxial (Hf,Zr)N/ScN metal/dielectric superlattices, ACS Appl. Energy Mater. 5, 3898 (2022).
- [29] M. A. Moram, M. J. Kappers, and C. J. Humphreys, Low dislocation density nonpolar (1120) GaN films achieved using scandium nitride interlayers, Phys. Status Solidi C 7, 1778 (2010).
- [30] M. A. Moram, Y. Zhang, M. J. Kappers, Z. H. Barber, and C. J. Humphreys, Dislocation reduction in gallium nitride films using scandium nitride interlayers, Appl. Phys. Lett. 91, 152101 (2007).

- [31] P. John, A. Trampert, D. Van Dinh, D. Spallek, J. Lähnemann, V. M. Kaganer, L. Geelhaar, O. Brandt, and T. Auzelle, ScN/GaN(1100): A new platform for the epitaxy of twinfree metal–semiconductor heterostructures, Nano Lett. 24, 6233 (2024).
- [32] F. Tasnádi, B. Alling, C. Höglund, G. Wingqvist, J. Birch, L. Hultman, and I. A. Abrikosov, Origin of the anomalous piezo-electric response in wurtzite Sc<sub>x</sub>Al<sub>1-x</sub>N alloys, Phys. Rev. Lett. **104**, 137601 (2010).
- [33] R. Guido, T. Mikolajick, U. Schroeder, and P. D. Lomenzo, Role of defects in the breakdown phenomenon of Al<sub>1-x</sub>Sc<sub>x</sub>N: From ferroelectric to filamentary resistive switching, Nano Lett. **23**, 7213 (2023).
- [34] S. Fichtner, N. Wolff, F. Lofink, L. Kienle, and B. Wagner, AlScN: A III-V semiconductor based ferroelectric, J. Appl. Phys. 125, 114103 (2019).
- [35] M. Uehara, R. Mizutani, S. Yasuoka, T. Shiraishi, T. Shimizu, H. Yamada, M. Akiyama, and H. Funakubo, Demonstration of ferroelectricity in ScGaN thin film using sputtering method, Appl. Phys. Lett. 119, 172901 (2021).
- [36] M. Akiyama, T. Kamohara, K. Kano, A. Teshigahara, Y. Takeuchi, and N. Kawahara, Enhancement of piezoelectric response in scandium aluminum nitride alloy thin films prepared by dual reactive cosputtering, Adv. Mater. 21, 593 (2009).
- [37] S. Karki, V. Rogers, P. Jadaun, D. S. Marshall, and J. A. C. Incorvia, Large magnetoresistance in scandium nitride magnetic tunnel junctions using first principles, Adv. Theory Simul. 4, 2100309 (2021).
- [38] T. Ohgaki, K. Watanabe, Y. Adachi, I. Sakaguchi, S. Hishita, N. Ohashi, and H. Haneda, Electrical properties of scandium nitride epitaxial films grown on (100) magnesium oxide substrates by molecular beam epitaxy, J. Appl. Phys. 114, 093704 (2013).
- [39] S. Rudra, D. Rao, S. Poncé, and B. Saha, Dominant scattering mechanisms in limiting the electron mobility of scandium nitride, Nano Lett. **24**, 11529 (2024).
- [40] D. Rao, B. Biswas, E. Flores, A. Chatterjee, M. Garbrecht, Y. R. Koh, V. Bhatia, A. I. K. Pillai, P. E. Hopkins, M. Martin-Gonzalez, and B. Saha, High mobility and high thermoelectric power factor in epitaxial ScN thin films deposited with plasma-assisted molecular beam epitaxy, Appl. Phys. Lett. 116, 152103 (2020).
- [41] B. Saha, M. Garbrecht, J. A. Perez-Taborda, M. H. Fawey, Y. R. Koh, A. Shakouri, M. Martin-Gonzalez, L. Hultman, and T. D. Sands, Compensation of native donor doping in ScN: Carrier concentration control and *p*-type ScN, Appl. Phys. Lett. **110**, 252104 (2017).
- [42] S. Nayak, M. Baral, M. Gupta, J. Singh, M. Garbrecht, T. Ganguli, S. M. Shivaprasad, and B. Saha, Rigid-band electronic structure of scandium nitride across the *n*-type to *p*-type carrier transition regime, Phys. Rev. B 99, 161117 (2019).
- [43] S. Rudra, D. Rao, S. Poncé, and B. Saha, Reversal of band-ordering leads to high hole mobility in strained *p*-type scandium nitride, Nano Lett. **23**, 8211 (2023).
- [44] D. Rao, D. P. Panda, A. I. K. Pillai, A. Tayal, M. Garbrecht, and B. Saha, Quasiclassical Anderson transition and thermally activated percolative charge transport in single-crystalline ScN, Phys. Rev. B 109, 155307 (2024).

- [45] Y. Kumagai, N. Tsunoda, and F. Oba, Point defects and p-type doping in ScN from first rinciples, Phys. Rev. Appl. 9, 034019 (2018).
- [46] M. Matsubara and E. Bellotti, A first-principles study of carbon-related energy levels in GaN. I. Complexes formed by substitutional/interstitial carbons and gallium/nitrogen vacancies, J. Appl. Phys. 121, 195701 (2017).
- [47] J. L. Lyons, D. Wickramaratne, and C. G. Van de Walle, A first-principles understanding of point defects and impurities in GaN, J. Appl. Phys. 129, 111101 (2021).
- [48] D. O. Demchenko, I. C. Diallo, and M. A. Reshchikov, Hydrogen-carbon complexes and the blue luminescence band in GaN, J. Appl. Phys. 119, 035702 (2016).
- [49] S. Wu, X. Yang, H. Zhang, L. Shi, Q. Zhang, Q. Shang, Z. Qi, Y. Xu, J. Zhang, N. Tang, X. Wang, W. Ge, K. Xu, and B. Shen, Unambiguous identification of carbon location on the N site in semi-insulating GaN, Phys. Rev. Lett. 121, 145505 (2018).
- [50] A. J. E. Rowberg, S. Mu, and C. G. Van de Walle, First-principles study of hydrogen- and oxygen-related complexes in ScN, J. Appl. Phys. 135, 125701 (2024).
- [51] See Supplemental Material at http://link.aps.org/supplemental/ 10.1103/b5x8-c1bl for experimental details and additional information
- [52] D. M. Phase, M. Gupta, S. Potdar, L. Behera, R. Sah, and A. Gupta, Development of soft x-ray polarized light beamline on Indus-2 synchrotron radiation source, AIP Conf. Proc. 1591, 685 (2014).
- [53] Ł. Haryński, A. Olejnik, K. Grochowska, and K. Siuzdak, A facile method for Tauc exponent and corresponding electronic transitions determination in semiconductors directly from UV– Vis spectroscopy data, Opt. Mater. 127, 112205 (2022).
- [54] P. Giannozzi, S. Baroni, N. Bonini, M. Calandra, R. Car, C. Cavazzoni, D. Ceresoli, G. L. Chiarotti, M. Cococcioni, I. Dabo, A. Dal Corso, S. De Gironcoli, S. Fabris, G. Fratesi, R. Gebauer, U. Gerstmann, C. Gougoussis, A. Kokalj, M. Lazzeri, L. Martin-Samos *et al.*, QUANTUM ESPRESSO: A modular and open-source software project for quantum simulations of materials, J. Phys. Condens. Matter 21, 395502 (2009).
- [55] P. E. Blöchl, Projector augmented-wave method, Phys. Rev. B 50, 17953 (1994).
- [56] J. P. Perdew, K. Burke, and M. Ernzerhof, Generalized gradient approximation made simple, Phys. Rev. Lett. 77, 3865 (1996).
- [57] S. L. Dudarev, G. A. Botton, S. Y. Savrasov, C. J. Humphreys, and A. P. Sutton, Electron-energy-loss spectra and the structural stability of nickel oxide: An LSDA+U study, Phys. Rev. B 57, 1505 (1998).
- [58] B. Himmetoglu, R. M. Wentzcovitch, and M. Cococcioni, First-principles study of electronic and structural properties of CuO, Phys. Rev. B 84, 115108 (2011).
- [59] N. Marzari, D. Vanderbilt, A. De Vita, and M. C. Payne, Thermal contraction and disordering of the Al(110) surface, Phys. Rev. Lett. 82, 3296 (1999).
- [60] S. Zhang and J. Northrup, Chemical potential dependence of defect formation energies in GaAs: Application to Ga selfdiffusion, Phys. Rev. Lett. 67, 2339 (1991).
- [61] R. Kumar, L. Yang, I. Mccarroll, S. M. Shivaprasad, J. M. Cairney, M. Garbrecht, and B. Saha, Atomistic structure and three-dimensional spatial distribution of oxide clusters along voids in nitride metal/semiconductor superlattices, Phys. Rev. Mater. 5, 084601 (2021).

- [62] J. Heyd, G. E. Scuseria, and M. Ernzerhof, Hybrid functionals based on a screened Coulomb potential, J. Chem. Phys. 118, 8207 (2003).
- [63] J. Heyd, G. E. Scuseria, and M. Ernzerhof, Erratum: "Hybrid functionals based on a screened Coulomb potential" [J. Chem. Phys. 118, 8207 (2003)], J. Chem. Phys. 124, 219906 (2006).
- [64] G. Kresse and D. Joubert, From ultrasoft pseudopotentials to the projector augmented-wave method, Phys. Rev. B 59, 1758 (1999).
- [65] G. Kresse and J. Furthmüller, Efficient iterative schemes for ab initio total-energy calculations using a plane-wave basis set, Phys. Rev. B 54, 11169 (1996).
- [66] Y. Kumagai, N. Tsunoda, A. Takahashi, and F. Oba, Insights into oxygen vacancies from high-throughput first-principles calculations, Phys. Rev. Mater. 5, 123803 (2021).
- [67] N. Tsunoda, Y. Kumagai, A. Takahashi, and F. Oba, Electrically benign defect behavior in zinc tin nitride revealed from first principles, Phys. Rev. Appl. 10, 011001 (2018).
- [68] Y. Kumagai, K. Harada, H. Akamatsu, K. Matsuzaki, and F. Oba, Carrier-induced band-gap variation and point defects in Zn<sub>3</sub>N<sub>2</sub> from first principles, Phys. Rev. Appl. 8, 014015 (2017).
- [69] R. Mojumder, Rayid-Mojumder/GaN\_Point\_Defect\_Investigation\_with\_DFT\_VASP-PyDefect: V1.0.0, Zenodo (2025), doi: 10.5281/zenodo.15358398.
- [70] J. P. Perdew and A. Zunger, Self-interaction correction to density-functional approximations for many-electron systems, Phys. Rev. B 23, 5048 (1981).
- [71] D. M. Ceperley and B. J. Alder, Ground state of the electron gas by a stochastic method, Phys. Rev. Lett. 45, 566 (1980).
- [72] J. L. Lyons and C. G. Van de Walle, Computationally predicted energies and properties of defects in GaN, npj Comput. Mater. 3, 12 (2017).
- [73] H. Li, M. Huang and S. Chen, First-principles exploration of defect-pairs in GaN, J. Semicond. 41, 032104 (2020).
- [74] H. J. Monkhorst and J. D. Pack, Special points for Brillouinzone integrations, Phys. Rev. B 13, 5188 (1976).
- [75] Y. Kumagai and F. Oba, Electrostatics-based finite-size corrections for first-principles point defect calculations, Phys. Rev. B 89, 195205 (2014).
- [76] C. Freysoldt, J. Neugebauer, and C. G. Van de Walle, Fully *ab initio* finite-size corrections for charged-defect supercell calculations, Phys. Rev. Lett. **102**, 016402 (2009).
- [77] J. J. Rehr, J. J. Kas, F. D. Vila, M. P. Prange, and K. Jorissen, Parameter-free calculations of x-ray spectra with FEFF9, Phys. Chem. Chem. Phys. **12**, 5503 (2010).
- [78] N. Tureson, M. Marteau, T. Cabioch, N. Van Nong, J. Jensen, J. Lu, G. Greczynski, D. Fournier, N. Singh, A. Soni, L. Belliard, P. Eklund, and A. Le Febvrier, Effect of ion-implantation-induced defects and Mg dopants on the thermoelectric properties of ScN, Phys. Rev. B 98, 205307 (2018).
- [79] R. Burcea, H. Bouteiller, S. Hurand, P. Eklund, J. F. Barbot, and A. le Febvrier, Effect of induced defects on conduction mechanisms of noble-gas-implanted ScN thin films, J. Appl. Phys. 134, 055107 (2023).
- [80] R. Burcea, J. F. Barbot, P. O. Renault, D. Eyidi, T. Girardeau, M. Marteau, F. Giovannelli, A. Zenji, J. M. Rampnoux, S. Dilhaire, P. Eklund, and A. Le Febvrier, Influence of generated defects by

- Ar implantation on the thermoelectric properties of ScN, ACS Appl. Energy Mater. **5**, 11025 (2022).
- [81] B. Saha, J. A. Perez-Taborda, J.-H. Bahk, Y. R. Koh, A. Shakouri, M. Martin-Gonzalez, and T. D. Sands, Temperature-dependent thermal and thermoelectric properties of *n*-type and *p*-type Sc<sub>1-x</sub>Mg<sub>x</sub>N, Phys. Rev. B **97**, 085301 (2018).
- [82] https://www.webelements.com.
- [83] H. Rassaerts, H. Nowotny, G. Vinek, and F. Benesovsky, On the scandium-carbon system, 1st part, Monatshefte für Chemie Chem. Mon. **98**, 460 (1967).
- [84] H. A. Al-Brithen, A. R. Smith, and D. Gall, Surface and bulk electronic structure of ScN(001) investigated by scanning tunneling microscopy/spectroscopy and optical absorption spectroscopy, Phys. Rev. B **70**, 045303 (2004).

- [85] S. Mu, A. J. E. Rowberg, J. Leveillee, F. Giustino, and C. G. Van de Walle, First-principles study of electron transport in ScN, Phys. Rev. B **104**, 075118 (2021).
- [86] M. G. Moreno-Armenta and G. Soto, Electronic structure of scandium nitride with nitrogen and scandium deficits, Comput. Mater. Sci. 40, 275 (2007).
- [87] J. J. Yeh and I. Lindau, Atomic subshell photoionization cross sections and asymmetry parameters:  $1 \le Z \le 103$ , At. Data Nucl. Data Tables **32**, 1 (1985).
- [88] J. L. Lyons, A. Janotti, and C. G. Van de Walle, Effects of carbon on the electrical and optical properties of InN, GaN, and AlN, Phys. Rev. B **89**, 035204 (2014).
- [89] D. Mukhopadhyay, S. Rudra, B. Biswas, P. Das, and B. Saha, Surface scattering-dependent electronic transport in ultrathin scandium nitride films, Appl. Phys. Lett. 123, 192101 (2023).